Atomistic study of the fcc → bcc transformation in a binary system: Insights from the Quasi-particle Approach

Gilles Demange, M. Lavrskyi, K. Chen, X. Chen, Z.D. Wang, Renaud Patte, Helena Zapolsky

Version of Record: https://www.sciencedirect.com/science/article/pii/S1359645421009770
Manuscript_649d2c4bf57e862bbf2b5eba4fb4245e

Atomistic study of the fcc→bcc transformation in a binary system: insights from the Quasi-particle Approach

G. Demange[a], M. Lavrskyi[a], K. Chen[b], X. Chen[c], Z. D. Wang[b,c], R. Patte[a], H. Zapolsky[a]

[a] *GPM, UMR CNRS 6634, Université de Rouen-Normandy, 76575 Saint Étienne du Rouvray, France*
[b] *School of Materials Science and Engineering, University of Science and Technology Beijing, Beijing 100083, P.R.China*
[c] *State Key Laboratory for Advanced Metals and Materials, University of Science and Technology Beijing, Beijing 100083, P.R.China*

Abstract

In this work, the Quasi-particle Approach (QA) is applied to qualitatively reproduce the underlying mechanisms of the displacive fcc (γ) → bcc (α) transformation. At the microstructural scale, we demonstrate that the QA is able to predict the growth of a bcc nucleus in a fcc matrix, and the eventual formation of an internally twinned structure consisting in two variants with Kurdjumov-Sachs orientation relationship. At the atomic level, the defect structure of twinning boundaries and fcc/bcc interfaces is identified, and the main mechanism for the propagation of the fcc/bcc interface is analyzed. In detail, it is confirmed that twin boundaries are propagated by the glide of pairs of partial twin dislocations, while the propagation of fcc screw dislocations along coherent terrace edges is the pivotal vector of the fcc/bcc transformation. The simulation results are compared qualitatively with our TEM and HRTEM observations of Fe-rich bcc twinned particle embedded in the fcc Cu-rich matrix in the Cu-Fe-Co system.

Introduction

Displacive solid-state phase transformations from the face centered cubic (fcc) austenite phase (γ) to body centered cubic (bcc) ferrite phase (α) play a pivotal role in the physical properties of steels and ferrous alloys. It is characterized by a collective movement of a large number of atoms over a distance typically smaller than the interatomic distance. The rapid change in crystal structure inherently alters the mechanical properties of these materials, including fatigue, plasticity and strength, whence the early and thorough studies thereupon [1, 2, 3, 4, 5, 6, 7, 8, 9].

The present understanding of fcc→bcc transformation is based on the Phenomenological Theory of Martensite Crystallography (PTMC) [10, 11], which posits the existence of an invariant plane strain for the shape transformation [10, 11]. This is achieved by homogeneous deformations [12] giving rise to special Orientation Relationships (OR), and producing shape deformations manifesting themselves by a specific surface relief [13]. Aside from [4], the PTMC does not account for the atomic structure of the interface, and thus cannot explain the dislocation-based mechanisms fueling the propagation of the interface. This shortcoming was later addressed by the Topological Model (TM) [14, 7, 15], which describes the structure of the fcc/bcc interface in terms of periodic unit of coherent terraces reticulated by a network of glissile transformation dislocations [16, 17], and by the new theory of the fcc→bcc transformation hereafter proposed in [18].

In parallel, modeling and simulation tools proved useful to confirm, refine or even inspire [18] theoretical predictions, as well as predict microstructures resulting from martensitic transformations (MT). At the mesoscale, the phase-field model (PFM) [19] could reproduce the complex morphology and topological changes during MT transformations [20, 21]. At the atomic scale, molecular dynamics (MD) [8, 22] and Monte Carlo (MC) modeling [23, 24] significantly contributed to unravel the atomic structure and propagation mode of the fcc/bcc interface, and remain numerical tools of choice to study martensitic transformations. One distinct advantage of MD simulations comes from the existence of a large database of interatomic potentials that can be used to quantitatively study interface migration. Leveraging this asset, MD was used to simulate the fcc→bcc transformation [25] and evaluate the velocities, mobility and activation energy of austenite–ferrite interfaces [26, 9] in pure iron. It was also employed to understand the general mechanism for fcc/bcc interface propagation in steels [18], and prospect the coupling between diffusional creep, displacive dislocation nucleation, and grain rotation during nanoindentation and sintering [27]. The MD approach yet contends with several shortcomings. First,

URL: gilles.demange@univ-rouen.fr (G. Demange), wangzd@mater.ustb.edu.cn (Z. D. Wang)

the growth mechanisms provided by MD simulations [9] are strongly influenced by the choice of interatomic potential [28, 29, 30]. Second, albeit particularly suited to prospect the relaxation of fcc/bcc interfaces [18], MD approaches are limited to reproduce the dynamics of fcc→bcc transformations on large microstuctural units of several dozen nanometers, mainly due to computational limitations. In parallel, Kinetic Monte Carlo (KMC) methods notably allowed to identify the different propagation modes for the fcc/bcc interface [31]. Recently, mixed MC/MD models enabled to alleviate the timescale limitation of MD. In doing so, it was possible to investigate the nucleation a bcc phase from a fcc matrix [32] and the early stage of the growth of a Cr bcc precipitate in a Cu fcc matrix [33].

An alternative approach to MD and KMC to prospect fcc → bcc transformations at the atomic scale is provided by the atomic phase-field models (APFM) [34]. Atomic phase-field models can be sorted into two main families. On the one hand, the Phase-Field-Crystal (PFC) model was originally derived by Elder et al. [35, 36], upon using free-energy functionals that are minimized by periodic order parameters, the fluctuation of which are interpreted as atoms. It was then extended to binary systems [37], first curtailed to the bcc symmetry, thereupon expanded to arbitrary crystallography [38] under the banner of XPFC [39]. Recently, the PFC approach was developed to model diffusion-mediated plasticity and creep [40], dendrite growth and ternary alloys equilibrium properties [41], and stress induced grain boundary motion and solute drag [42]. The PFC model was also extended to binary system [43]. One salient principle of the 2-components (X)PFC, is to feature two spatially uncorrelated variables: the atomic density that sets the periodic crystal structure disregarding local composition fluctuations, and the coarse grain concentration of one component. This allowed to connect XPFC simulations to average thermodynamics data such as equilibrium phase diagrams [42]. However, the XPFC model does not take into account the difference in atomic radius of the components in binary systems, which hinders the reproduction of diffusion processes connected to atomic size effect. More generally, most PFC models are not equipped with short range interactions that set the size of atoms [44, 45, 46]. In parallel to the PFC models, an alternative APFM called the Quasi-particle Approach (QA) was developed in [47], where the ensemble averaged atomic occupation probability of each chemical species is considered. The potentials used in the QA are equipped with short range (SR) interactions that set the atomic radius for each species in multi-component systems, and long range (LR) interactions that can be defined in a more versatile manner than in most PFC models [48]. As a result, the QA can circumvent the usual numerical artifacts of PFC models, account for different atomic sizes, and permit the modeling of a wide range of structures at the atomic scale [48]. Among others, the QA was successful in modeling the structure of grain boundaries in the bcc iron phase [49, 50], the self-assembly of atoms into complex structures [47], as well as solute segregation in Fe-based alloys [51].

With this, the QA was selected in the present work to prospect the fcc→bcc transformation in a simplified 2-component precipitate/matrix system. For that purpose, two refinements were added to the QA. First, a new potential designed to reproduce the fcc→bcc structural transformation was implemented for the first time. Second, an original physically informed post-treatment approach was used to infer the positions of atomic centers from the atomic occupation probability fields provided as the raw output of QA simulations. This allowed to profit with the structural analysis tools of OVITO, and thereby strengthen the capacity of the QA to characterize complex defect structures emerging during the transformation.

The motivation of this work is to apply the QA to connect the atomistic mechanisms of the twinning fcc→bcc transformation to the microstructure dynamics on a large space scale. In doing so, this approach will fill the gap between large scale simulations based on coarse grained models such as the standard PFM, and focused simulations using atomistic approaches such as MD. A first qualitative comparison between the numerical results and present experimental observations of internally twinned Fe-rich bcc particles having the Kurdjumov-Sachs (KS) orientation relationships (ORs) in a Fe-Cu-Co alloy [52] is conducted, in order to challenge the model on a real study-case.

This study is organized as follows: first, the QA model presently developed for the fcc→bcc transformation in a binary system is introduced. Second, one large scale QA simulation of the fcc→bcc transformation in a precipitate from a hypercritical bcc nucleus is presented as the cornerstone of the paper. The morphology and the structure of the bcc inclusion are analyzed at the microstructural scale. Afterwards, twin boundaries are prospected, and the growth mode of twin variants is deciphered at the atomic level. Lastly, the surface relief of the fcc/bcc interface for an ellipsoidal bcc inclusion is characterized, whilst an interpretation of the propagation mechanism of the curved interface is proposed from the analysis of transformation dislocations. Finally, simulation results are compared with the experimental data obtained by TEM observations on an as cast Fe-Cu-Co alloy.

1. Numerical approach

In this section, the QA used in the present work is detailed. The numerical values of all model parameters are listed in table 1. Additional details on the QA, as well as the choice of numerical settings of parameters can be found in the Online Supplementary Material 1.

1.1. The Quasi-particle Approach (QA)

To describe the growth of the bcc particle in the fcc matrix in a binary system, the Quasi-particle Approach (QA) proposed in [47] was used. This method can be seen as extension of the seminal Atomic Density Function (ADF) theory first proposed in [53] to the continuum case. In the ADF theory, the atomic configuration of the system at a given time t is described by the value of an occupation probability $P(\boldsymbol{r}, t)$ on each lattice site $\boldsymbol{r}$ of an underlying Ising lattice I defined as a set of N_0 lattice sites: $I = \{\boldsymbol{r}\}$. The occupation probability $P(\boldsymbol{r}, t)$ represents the probability for a given lattice site $\boldsymbol{r}$ to be occupied by an atom at time t. The temporal evolution of these variables is governed by Onsager diffusion equations [53]. In the ADF approach, the probability function is specified at each site of I, which coincides with the simulation grid. This confines the application range of the model to isostructural phase transformations. It should be emphasized that this limitation is not specific to the ADF model, as it also penalizes other rigid lattice approaches, including the KMC [24] and SKMF [54, 55] models.

This shortcoming of the ADF theory was circumvented in the Continuum Atomic Density Function (CADF) theory [56] upon choosing the simulation grid spacing Δx several times smaller than the interatomic distance a ($\Delta x \ll a$). With this, the CADF allowed to account for the atomic movements in the continuous space, thereby making the model applicable to structural phase transitions. In the CADF framework, atoms are no longer points, but rather spheres of radius R containing a certain number of the simulation grid nodes. With this, a new interaction Hamiltonian should be defined to set the dynamics of the system. One such Hamiltonian was proposed in an upgrade of the CADF model referred to as Quasi-particle Approach (QA) [47]. Therein, the displacements of atoms can be associated to the creation and annihilation of non-traditional dynamic variables called fratons on each grid node.

With this, a m-components system can be characterized by the values of m stochastic numbers $c_\alpha(\boldsymbol{r})$ in each lattice site $\boldsymbol{r}$, where $\alpha = 1, 2, ..m$ labels the fratons corresponding to atoms of atomic species α. Here, m is the number of different atomic species. Occupation variables c_α are then averaged over the time-dependent Gibbs ensemble of fratonic configurations into the occupation probability $\rho_\alpha(\boldsymbol{r}, t) \equiv \langle c_\alpha(\boldsymbol{r}, t)\rangle$, where the $\langle\cdot\rangle$ symbol denotes the Gibbs ensemble average at temperature T over a time t. With this definition, the function $\rho_\alpha(\boldsymbol{r}, t)$ is the probability that a lattice point in site $\boldsymbol{r}$ is located anywhere inside the atomic sphere of an atom of kind α at time t. Therefore, the atomic configuration of the system can be fully described by the density function $\rho_\alpha(\boldsymbol{r}, t)$, for $\alpha = 1, \ldots, m$. Moreover, the temporal evolution of the system is given by the microscopic diffusion equation:

$$\frac{\partial \rho_\alpha}{\partial t}(\boldsymbol{r}, t) = \sum_{\beta=1}^{m} \sum_{\boldsymbol{r}' \in I} L_{\alpha\beta}(\boldsymbol{r} - \boldsymbol{r}') \frac{\delta F}{\delta \rho_\beta(\boldsymbol{r}', t)}, \tag{1}$$

where the summation is carried out over the the number N_0 of grid lattice sites $\boldsymbol{r}$ of the Ising lattice I. In equation 1, $L_{\alpha\beta}(\boldsymbol{r} - \boldsymbol{r}')$ is the matrix of kinetic coefficients between fratons of kind α and β ($\alpha, \beta = 1, 2, ..m$), and F is the non-equilibrium Helmholtz free energy functional. The kinetic equation 1 approximates the evolution rate of the density functions $\rho_\alpha(\boldsymbol{r}, t)$ by the first non-vanishing term of its expansion with respect to the thermodynamic driving force. This microscopic diffusion equation is strongly nonlinear with respect to the density field $\rho_\alpha(\boldsymbol{r}, t)$, but it is linear with respect to the chemical driving force. To guarantee the conservation of the total number of fratons of kind α, the kinetic coefficients matrix should satisfy the following condition for all $\alpha, \beta = 1, \ldots, m$:

$$\sum_{\boldsymbol{r} \in I} L_{\alpha\beta}(\boldsymbol{r}) = 0. \tag{2}$$

Each grid node can be occupied by a fraton of type $\alpha = 1, \ldots, m$, or by no fraton (empty site V). Then, according to the conservation condition $\sum_{\alpha=1}^{m} \rho_\alpha(\boldsymbol{r}, t) + \rho_V(\boldsymbol{r}, t) = 1$, where ρ_V is the probability that a lattice site is not occupied by a fraton, only m fraton density functions should effectively be defined to describe the fratonic configuration of the m-components system. The free energy F of the system is defined under mean-field

approximation by:

$$F = \sum_{\alpha=1}^{m} \sum_{\substack{\beta=1 \\ \beta \geq \alpha}}^{m} \left[\frac{1}{2} \sum_{\boldsymbol{r},\boldsymbol{r}' \in I} W_{\alpha\beta}(\boldsymbol{r}-\boldsymbol{r}') \rho_\alpha(\boldsymbol{r},t) \rho_\beta(\boldsymbol{r}',t) \right] \\ + k_B T \sum_{\boldsymbol{r} \in I} \left[\sum_{\alpha=1}^{m} \rho_\alpha(\boldsymbol{r},t) \ln(\rho_\alpha(\boldsymbol{r},t)) + \left(1 - \sum_{\alpha=1}^{m} \rho_\alpha(\boldsymbol{r},t)\right) \ln\left(1 - \sum_{\alpha=1}^{m} \rho_\alpha(\boldsymbol{r},t)\right) \right]. \tag{3}$$

Here, k_B is the Boltzmann constant and T is the temperature. Moreover, the first and second terms on the right-hand side of the equality respectively correspond to the internal energy and the configurational entropy. $W_{\alpha\beta}$ is the pairwise interaction potential between fratons of type α and β separated by a distance $|\boldsymbol{r}-\boldsymbol{r}'|$. According to [57], the model fraton-fraton pair potential $W_{\alpha\beta}$ embodies the so-called short range (SR) and long range (LR) interactions, respectively written θ_α and $W^{\mathrm{LR}}_{\alpha\beta}$:

$$W_{\alpha\beta}(\boldsymbol{r}-\boldsymbol{r}') = \theta_\alpha(\boldsymbol{r}-\boldsymbol{r}')\delta_{\alpha\beta} + \lambda_{\alpha\beta} W^{\mathrm{LR}}_{\alpha\beta}(\boldsymbol{r}-\boldsymbol{r}'). \tag{4}$$

Here, $\delta_{\alpha\beta}$ is the Kronecker delta function. For interactions between fratons of the same atomic species ($\alpha = \beta$), $\lambda_{\alpha\alpha}$ is the relative amplitude between LR and SR interactions. The setting of this parameter should ensure that atoms have a specific finite size on the one hand, while keeping LR interactions sufficiently strong to reproduce the desired crystallographic structure on the other hand. In this work, we chose to use a single value $\lambda_{\alpha\alpha} \equiv \lambda = 0.2$ for all components $\alpha = 1, \ldots, m$. Regarding cross interactions ($\alpha \neq \beta$), no SR interactions are considered in the present work ($\delta_{\alpha\beta} = 0$ for $\alpha \neq \beta$), so that $W_{\alpha\beta} \equiv \lambda_{\alpha\beta} W^{\mathrm{LR}}_{\alpha\beta}$. For this reason, the setting of $\lambda_{\alpha\beta}$ for $\alpha \neq \beta$ is not connected to the size of atoms, but rather to the intensity of chemical interactions between different species. It should thus be set only after the atomic species are selected, and the functional form of $W^{\mathrm{LR}}_{\alpha\beta}$ is provided. This is done in the following.

In detail, the SR contribution θ_α allows the spontaneous condensation of fratons into atomic spheres, and prevents the overlap or atoms. To describe SR interactions, the step function depicted in 1(a) was used [47]:

$$\theta_\alpha(\boldsymbol{r}) = \begin{cases} -1 & \text{if} \quad r \leq R_\alpha \\ \xi & \text{if} \quad R_\alpha < r \leq R_\alpha + \Delta R_\alpha \\ 0 & \text{otherwise.} \end{cases} \tag{5}$$

Here, R_α sets the width of the attractive part of the SR potential, which allows the condensation of fratons into atomic spheres. It is thus liken to the radius of atomic spheres for component α. Then, ΔR_α and ξ are respectively the width of the SR potential barrier for each component α, and the height of this barrier. It should be noted that ξ was chosen equal for each component α. The introduction of a repulsive contribution in the SR potential not only prevents the overlap of atomic spheres, but also contributes to adjust the elastic properties of the system. In this work, we chose $\xi = 4.0$ for the barrier height, and $\Delta R_\alpha = 0.17 R_\alpha$ for the barrier width. The numerical setting of R_α (and thus ΔR_α) depends on the lattice parameters and crystallographic structure of each component α. It is thus provided in the following, after the crystallographic structures and lattice parameters are selected.

For purposes of computational efficiency, the interaction potential $W_{\alpha\beta}$ is implemented in reciprocal space by means of the Fourier transforms $\hat{\theta}_\alpha(\boldsymbol{k})$ and $\hat{W}^{\mathrm{LR}}_{\alpha\beta}(\boldsymbol{k})$ of the SR and LR interactions respectively, where $\boldsymbol{k}$ is the k-vector defined by $\boldsymbol{k} = (k_x, k_y, k_z) = \frac{2\pi}{N}(h,k,l)$ with (h,k,l) being dimensionless coordinates in three dimensions, and N the size of the cubic simulation box (number of grid nodes on each edge of the simulation domain, so that the total number of grid nodes is $N_0 = N^3$). The functional form in Fourier space of the LR interaction potentials can only be written for a specific crystallographic structure. It is provided in the following (see formula 8). In Fourier space, the total interaction potential introduced in equation 4 then reads:

$$\hat{W}_{\alpha\beta}(\boldsymbol{k}) = \hat{\theta}_\alpha(\boldsymbol{k})\delta_{\alpha\beta} + \lambda_{\alpha\beta} \hat{W}^{\mathrm{LR}}_{\alpha\beta}(\boldsymbol{k}), \tag{6}$$

where we recall that $\lambda_{\alpha\alpha} \equiv \lambda$. The Fourier transformation $\hat{\theta}_\alpha(\boldsymbol{k})$ of $\theta_\alpha(\boldsymbol{r})$ can be written:

$$\hat{\theta}_\alpha(k) = \frac{4\pi}{k^3} \big[-\sin(kR_\alpha) + kR_\alpha \cos(kR_\alpha) + \xi \big\{ \sin(k(R_\alpha + \Delta R_\alpha)) - k(R_\alpha + \Delta R_\alpha) \cos(k(R_\alpha + \Delta R_\alpha)) \\ - \sin(kR_\alpha) + kR_\alpha \cos(kR_\alpha) \big\} \big]. \tag{7}$$

The corresponding profile of $\hat{\theta}_\alpha(\boldsymbol{k})$ is displayed in figure 1(b).

For $\alpha = \beta$, the long range interaction potentials $\hat{W}^{\mathrm{LR}}_{\alpha\alpha}(\boldsymbol{k})$ sets the crystal structures for components $\alpha = 1, \ldots, m$, and influences the corresponding elastic properties to a large extent. Then, the cross interaction potentials $\hat{W}^{\mathrm{LR}}_{\alpha\beta}(\boldsymbol{k})$ control the chemical interactions between atoms of atomic species $\alpha \neq \beta$ in the system. In this work, isotropic spherical potentials were used as a mean to allow the formation of crystallographic structures with arbitrary orientation.

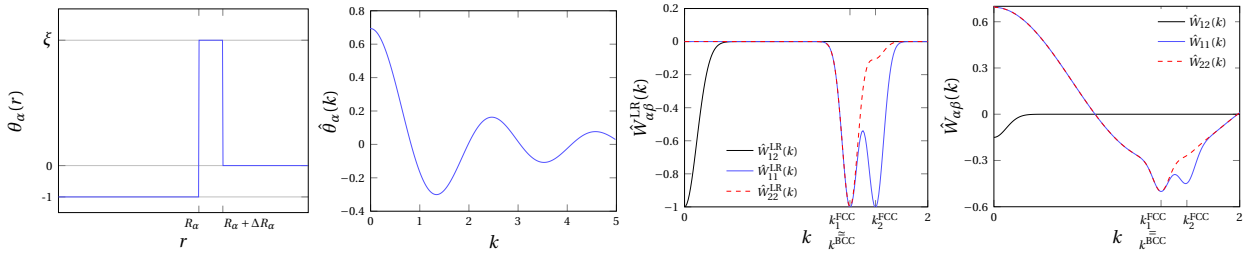

(a) $\theta_\alpha(r)$ (b) $\hat{\theta}_\alpha(k)$ (c) $\hat{W}^{\mathrm{LR}}_{\alpha\beta}$ (d) $\hat{W}_{\alpha\beta}$

Figure 1: Pairwise interaction potentials used in this work: (a) short range interaction potential in real space $\theta_\alpha(r)$ (for both components), (b) short range interaction potential in Fourier space $\hat{\theta}_\alpha(k)$, (c) long range interaction potentials $\hat{W}^{\mathrm{LR}}_{\alpha\beta}$, (d) complete interaction potentials $\hat{W}_{\alpha\beta}$, using parameters $a_1 = 8\Delta x$, $a_2 = 6.5\Delta x$, $R_\alpha = 2.81\Delta x$, $\Delta R_\alpha = 0.48\Delta x$, $\xi = 4$, $\sigma_1^{\mathrm{fcc}} = \sigma_2^{\mathrm{fcc}} = \sigma^{\mathrm{bcc}} = \sigma^{12} = 0.09$, $\lambda = 0.2$, and $\lambda_{12} = 0.15$. In c) and d), red dashes: component 2 (bcc), blue: component 1 (fcc), black: chemical interactions between component 1 and component 2 atoms.

In this study, we propose a toy model of immiscible binary alloy ($m = 2$), aiming at reproducing the displacive fcc→bcc structural transition in a precipitate/matrix binary system. Component 1 will henceforth pertain to the fcc matrix, and component 2 to the precipitate undergoing the fcc→bcc transformation. We also introduce two lattice parameters a_1 and a_2. The first lattice parameter a_1 refers to the fcc structure for both the fcc matrix (component 1), and the initial fcc structure of the precipitate (component 2). The second lattice parameter a_2 is the lattice parameter of the bcc structure of the precipitate (component 2). a_1 and a_2 were chosen as $a_1 = 8.0\Delta x$ and $a_2 = 6.5\Delta x$ respectively. This setting appeared as a good compromise between computational cost on the one hand, and a yield between a_1 and a_2 that was sufficiently close to $\sqrt{3/2}$, which corresponds to the conservation of the atomic volume between the bcc and fcc phases on the other hand. This setting comes with the lattice misfit $\delta_{\mathrm{fcc/bcc}} \equiv |a_1 - \sqrt{3/2}a_2|/a_1 = 0.0049$ between fcc and bcc phases, corresponding to the yield $a_1/a_2 = 1.23$ (a zero misfit corresponds to the yield $a_1/a_2 = \sqrt{3/2} \simeq 1.22$). This misfit is underestimated compared to its experimental counterparts (see [7, 18] and references therein): $\delta_{\mathrm{fcc/bcc}} \simeq 0.02 - 0.04$ corresponding to $a_1/a_2 = 1.25 - 1.27$ for pure iron and steels, and $\delta_{\mathrm{fcc/bcc}} \simeq 0.03$ corresponding to $a_1/a_2 = 1.26$ between bcc iron and fcc copper [58]). It should be noted that the deviation between the numerical and experimental values of the misfit results in a different elastic strain undergone by the transformed particle. This can in turn influence the shape of the bcc inclusion and its habit plane [13]. However, we assumed that the present version of the QA should be able to reproduce the underlying mechanisms of the fcc→bcc transformation and twinning formation. This hypothesis is supported by previous MD simulations performed for various OR and lattice misfits in [18]. Based on these numerical results, it was shown that the fcc→bcc transformation was carried by a unique set of defect structures, disregarding the precise value of the lattice misfit.

After setting the values of the lattice parameters a_1 and a_2, the atomic radius R_1 and R_2, and the corresponding widths ΔR_1 and ΔR_2 of the potential barrier in the definition 5 of SR interaction potentials θ_1 and θ_2 could also be fixed, based on the minimal distance between first next-neighbors for the considered crystallography. Recalling that this distance is equal to $d_{\mathrm{fcc}} = a_1\sqrt{2}/2$ in the fcc structure, and $d_{\mathrm{bcc}} = a_2\sqrt{3}/2$ in the bcc structure, then the following conditions hold: $R_1 \leq a_1\sqrt{2}/4 \simeq 2.828\Delta x$ (fcc structure) and $R_2 \leq a_2\sqrt{3}/4 \simeq 2.814\Delta x$ (bcc structure). For this reason, we set $R_1 = R_2 = 2.81\Delta x$ in this work. It follows that $\Delta R_1 = \Delta R_2 = 0.17R_1 = 0.48\Delta x$.

In this study, only spherically symmetric potentials were used for the LR interaction potential, as a mean to allow the formation of local clusters of different metastable phases with any orientations. Choice was made to use linear combinations of Gaussian functions. In the general case, the number of minima equipping the LR potential should be equal to the number of non-equivalent structural reflections in the first Brillouin zone of a given crystallographic structure. The reciprocal lattice of the fcc crystal is the bcc structure with the reciprocal lattice parameter $4\pi/a_1$. For this crystallography, two non-equivalent structural reflections can be found in the first Brillouin zone, with the same number of diffraction spots. These are located in $k_1^{\mathrm{fcc}} = \frac{2\pi\sqrt{3}}{a_1}$ and $k_2^{\mathrm{fcc}} = \frac{4\pi}{a_1}$. Therefore, the LR interaction potential $\hat{W}^{\mathrm{LR}}_{11}(k)$ for the fcc structure was equipped with two wells of equal

depth, respectively located in $k_1^{\mathrm{fcc}} = \frac{2\pi\sqrt{3}}{a_1} \simeq 1.360$ and $k_2^{\mathrm{fcc}} = \frac{4\pi}{a_1} \simeq 1.571$. Besides, the reciprocal lattice of the bcc crystal is the fcc structure with the reciprocal lattice parameter $4\pi/a_2$. It was shown in [35] and [47] that only one minima could be used for the bcc structure. The LR potential $\hat{W}_{22}^{\mathrm{LR}}(k)$ for the bcc structure was thus equipped with one well centered in $k^{\mathrm{bcc}} = \frac{2\pi\sqrt{2}}{a_2} \simeq 1.367$ in a first time. However, the initial fcc structure within the precipitate is strongly unstable with respect to the bcc structure when the pure bcc potential is used and infinitesimal fluctuations of the occupation probability field ρ_2 can trigger the fcc $\rightarrow$ bcc transformation far from the transition front. To prevent this instability, an additional well located in k_2^{fcc} was adjoined to $\hat{W}_{22}^{\mathrm{LR}}(k)$, in order to make the fcc structure for component 2 metastable. For that purpose, the amplitude of this second well was chosen smaller than that of the first well of $\hat{W}_{22}^{\mathrm{LR}}(k)$. To achieve this, the depth of this additional well was controlled by a multiplicative factor ϵ. This parameter should satisfy $0 < \epsilon < 1$ to ensure that the bcc structure has a lower value of chemical potential than the fcc phase, which is the driving force for the fcc $\rightarrow$ bcc transformation in the QA, while preserving the metastability of the fcc phase. However, small (but non zero) values of ϵ are better indicated, insofar as choosing ϵ too close to 1 can significantly slow down the transformation. In this work, ϵ was set to 0.1. It should be noted that the choice of ϵ has no sensitive impact on the simulated structure. However, because it modifies the driving force of the fcc $\rightarrow$ bcc transformation, it may affect the transformation rate. This point is beyond the scope of the present work, and will not be further discussed here.

To mimic the immiscibility of components 1 and 2, a repulsive cross interaction potential $\hat{W}_{12}^{\mathrm{LR}}(k)$ was used, which can be related to the mixing energy of the binary system. It is defined as a simple Gaussian function centered in $k = 0$, allowing the phase separation of the different chemical species. It should yet be noted that more sophisticated cross interaction potential functionals were previously developed in the framework of the QA. For instance, anisotropic potentials based on cluster functions with tetrahedral direction of bonds were implemented to model the formation of the zinc-blende structure in [47]. For the present case, a possible upgrade of the cross interaction term might involve a more quantitative estimation of copper-iron interactions by feeding the model with existing values of pair interaction energies. Then, the corresponding long range interaction potentials read:

$$\begin{cases} \hat{W}_{11}^{\mathrm{LR}}(k) = -\exp\left(-\dfrac{(k-k_1^{\mathrm{fcc}})^2}{2(\sigma_1^{\mathrm{fcc}})^2}\right) - \exp\left(-\dfrac{(k-k_2^{\mathrm{fcc}})^2}{2(\sigma_2^{\mathrm{fcc}})^2}\right) \\ \hat{W}_{22}^{\mathrm{LR}}(k) = -\exp\left(-\dfrac{(k-k^{\mathrm{bcc}})^2}{2(\sigma^{\mathrm{bcc}})^2}\right) - \epsilon\exp\left(-\dfrac{(k-k_2^{\mathrm{fcc}})^2}{2(\sigma_2^{\mathrm{fcc}})^2}\right) \\ \hat{W}_{12}^{\mathrm{LR}}(k) = -\exp\left(-\dfrac{k^2}{2(\sigma^{12})^2}\right). \end{cases} \tag{8}$$

In equation 8, the parameters σ_1^{fcc}, σ_2^{fcc}, and σ^{bcc} are the standard deviation of the different Gaussian wells. The choice of these parameters plays a prominent role in the fitting of the elastic properties of the material. The procedure used in the QA to connect the parameters σ_1^{fcc}, σ_2^{fcc}, and σ^{bcc} of the LR potential in equation 8 to the elastic constants of the bcc and fcc systems is detailed in the Online Supplementary Material 2. One should be aware that the tuning of other parameters stepping in the definition of the interaction potential (ξ, λ etc.) also have an influence on the elastic constants. However, because their influence is not restricted to the elastic constants, these parameters were fixed upstream, while the parameters σ_1^{fcc}, σ_2^{fcc}, and σ^{bcc} were chosen afterwards as $\sigma^{\mathrm{bcc}} = \sigma_1^{\mathrm{fcc}} = \sigma_2^{\mathrm{fcc}} = 0.09$, in order to keep the parameter setting of the model as simple as possible, while providing consistent elastic properties. Besides, the parameters σ^{12} sets the range of the chemical repulsion between component 1 and component 2. In this work, we also chose $\sigma^{12} = 0.09$. It should be noted that the system is only weakly sensitive to the choice of σ^{12}. The LR contributions to the interaction potential introduced in equation 8, using the parameter settings of table 1 are depicted in figures 1(c).

At this point, SR and LR contributions to the interaction potential are defined for the present 2-components system. Based on equations 6 and 8, and the previously selected value of λ, the interaction potentials $\hat{W}_{11}$ and $\hat{W}_{22}$ are thus fully defined. As for $\hat{W}_{12}$, we recall that $\hat{W}_{12} = \lambda_{12}\hat{W}_{12}^{\mathrm{LR}}$, so that λ_{12} should now be selected to unequivocally define $\hat{W}_{12}$. This parameter weights the relative influence of the structural contributions $\hat{W}_{11}$ $\hat{W}_{22}$ with respect to the chemical repulsion $\hat{W}_{12}^{\mathrm{LR}}$. Details on the correct setting of this parameter, and the normalization procedure of the potentials are provided in the Online Supplementary Material 1. In the present work, λ_{12} was set to 0.15. The full interaction potentials introduced in equation 6 using the parameter settings of table 1 are depicted in figure 1(d).

Using the procedure provided in the Online Supplementary Material 2 with the parameter setting summarized in table 1, the elastic moduli of the fcc and bcc structures could be calculated in reduced units. These are provided in the Appendix A. Rather than the absolute values of elastic constants in reduced units, the yield between the bulk modulus $B = (C_{11} + 2C_{12})/3$ of each phase, as well as Zener anisotropy parameter

$A = 2C_{44}/(C_{11} - C_{12})$ have a significant influence on the transformation. Here, indexing each parameter by the corresponding phase (bcc and fcc), we obtained $A^{\text{bcc}} = 1.3$ and $A^{\text{fcc}} = 3.1$, and $B^{\text{bcc}}/B^{\text{fcc}} = 1.4$. In this case, $A > 1$, and the elastically "soft" directions, which minimize the elastic energy, are $\langle 100 \rangle_\gamma$. Besides, the ratio between bulk modulus ensures that the bcc structure is harder than the fcc one. A qualitative comparison between QA simulations and experiments in a Fe-Cu-Co alloy displaying twinned iron-rich bcc precipitates in a copper fcc matrix is proposed in the last section of this study. While the elastic constants used in the QA are not fitted on their experimental counterpart in the Fe-Cu-Co alloy, Zener anisotropy parameters for the bcc and fcc structures in both the QA model and experiments are nonetheless greater than 1.0. This is thus qualitatively consistent with the experimental anisotropy parameter for bcc iron (~ 2.7) and fcc copper (~ 3.5) [59, 60]. Moreover, the yield between the bulk modulus of the bcc and fcc structures in the QA (1.4) is tantamount to the experimental values for bcc Fe/fcc Fe (1.27) and bcc Fe/fcc Cu (1.35) [59, 60]. However, this slightly overestimated difference between the elastic moduli of the bcc inclusion and the fcc parent phase in the present work might add up to the underestimated lattice mismatch to underestimate the inclusion relaxation energy contribution in the total elastic strain energy, and influence the morphology of the inclusion [13].

Simulations were performed in reduced units. The average density of probability $\bar{\rho}_{1,2}$ of type 1 and 2 atoms was defined as $4\pi R_{1,2}^3 N_{1,2}/(3V)$, where V is the total volume of the system ($V = (\Delta x N)^3$), and $N_{1,2}$ is the total number of atoms of type 1 and 2 at ground state. The input parameter in simulations was thus $\bar{\rho} = \bar{\rho}_1 + \bar{\rho}_2$. In the present work, $\bar{\rho}_1 = 0.0754$ and $\bar{\rho}_2 = 0.0546$, so that $\bar{\rho} = 0.13$. Moreover, $k_B T$ and ξ were expressed in $k_B T_m$ units, where T_m is the melting temperature of the system with composition $(\bar{\rho}_1, \bar{\rho}_2)$. The space scale was chosen as the grid spacing Δx, as set by the number of grid lattices spanning one lattice parameter. As for the time scale, it is measured in units $t^* = tL\Delta F$, where L is a kinetic coefficient for fraton displacements, and ΔF is the driving force of the transformation. One should bear in mind that the present work does not aim at providing the real time scale of this displacive phase transformation, as the latter lingers as a very challenging task for APFMs, but rather reproduce the metastable states along the kinetic path of the transition. The same reckoning applies to the standard PFM, which was yet successfully used to model displacive transformations before [20, 21, 61, 62]. Considering the optimized computational features of Fourier based numerical schemes, the kinetic equation 1 for the density probability functions $\rho_{1,2}$ was solved in Fourier space:

$$\begin{cases} \dfrac{\partial \hat{\rho}_1}{\partial t}(\boldsymbol{k},t) = \hat{\tilde{L}}_{11}(k)\left[\hat{W}_{11}(k)\hat{\rho}_1(\boldsymbol{k},t) + \hat{W}_{12}(k)\hat{\rho}_2(\boldsymbol{k},t) + k_B T\left\{\ln\left(\rho_1/(1-\rho_1-\rho_2)\right)\right\}_{\boldsymbol{k}}\right] \\ \qquad\qquad + \hat{\tilde{L}}_{12}(k)\left[\hat{W}_{22}(k)\hat{\rho}_2(\boldsymbol{k},t) + \hat{W}_{12}(k)\hat{\rho}_1(\boldsymbol{k},t) + k_B T\left\{\ln\left(\rho_2/(1-\rho_1-\rho_2)\right)\right\}_{\boldsymbol{k}}\right] \\ \dfrac{\partial \hat{\rho}_2}{\partial t}(\boldsymbol{k},t) = \hat{\tilde{L}}_{22}(k)\left[\hat{W}_{22}(k)\hat{\rho}_2(\boldsymbol{k},t) + \hat{W}_{12}(k)\hat{\rho}_1(\boldsymbol{k},t) + k_B T\left\{\ln\left(\rho_2/(1-\rho_1-\rho_2)\right)\right\}_{\boldsymbol{k}}\right] \\ \qquad\qquad + \hat{\tilde{L}}_{12}(k)\left[\hat{W}_{11}(k)\hat{\rho}_1(\boldsymbol{k},t) + \hat{W}_{12}(k)\hat{\rho}_2(\boldsymbol{k},t) + k_B T\left\{\ln\left(\rho_1/(1-\rho_1-\rho_2)\right)\right\}_{\boldsymbol{k}}\right], \end{cases} \tag{9}$$

where $\hat{\rho}_\alpha$ is the Fourier transform of the fraton density function ρ_α, $\{\cdot\}_{\boldsymbol{k}}$ is the discrete Fourier transform operator, and $\hat{L}_{11,22,12}(k) = -L^{\text{Ons}}_{11,22,12}k^2$. Details on the setting of Onsager diffusion coefficients are provided in the Online Supplementary Material 1. All parameters are compiled in reduced units in table 1.

$a_{1,2}$	$R_{1,2}$	$\Delta R_{1,2}$	ξ	λ	ϵ	$\sigma^{\text{fcc}}_{1,2}$	σ^{bcc}	σ^{12}	λ_{12}	$k_B T$	$\bar{\rho}$	$L^{\text{Ons}}_{11,22}$	L^{Ons}_{12}
8.0/6.5	2.81	0.48	4.0	0.2	0.1	0.09	0.09	0.09	0.15	0.11	0.13	1.0	0.5

Table 1: Parameters used in simulations.

To model the fcc to bcc phase transformation within the precipitate, the initial condition was chosen as a pure component 2 particle with perfect cubic shape embedded in a pure component 1 matrix with cube on cube OR. A small bcc nucleus was embedded in the center of the precipitate with KS OR with respect to the fcc phase. This initial condition was used as a mean to overcome the nucleation barrier of the bcc nucleus. The OR between the bcc nucleus and the fcc parent phase corresponded to the first Kurdjumov-Sachs (KS) variant V_1. The corresponding rotation matrix is provided in the Appendix B.

1.2. Numerical implementation and post-treatment of the QA

In this work, the length scale of the model was set to $\Delta x \simeq 0.045$ nm corresponding to the Fe-Cu alloy ($a_1 = 8.0\Delta x \sim 0.360$ nm, $a_2 = 6.5\Delta x \sim 0.293$ nm). In contrast, reduced time units were used considering the complex dependence of the time scale on the thermodynamic and kinetic parameters of the system. Simulations were performed in three dimensions on a 1024^3 grid lattice ($N = 1024$, so that the total number of points for the Ising lattice is $N_0 = N^3 = 1024^3$) equipped with periodic boundary conditions (PBC). For the chosen length

scale Δx, this corresponds to a volume of $(46\text{ nm})^3$. The kinetic equations 9 were solved by the Spectral-Eyre scheme [63], with the reduced time step $\Delta t = 0.005$, on 512 cores of the supercomputer CRIANN of Normandy. A computational advantage of the QA is to use a fully spectral approach on the one hand, and interaction potentials relying on pair correlation functions on the other hand. This makes the approach highly suitable for the MPI parallelization procedure, notably thanks to the FFTW subroutine [64]. It should nonetheless be mentioned that the Fourier-spectral approach requires specific boundary conditions such as periodic boundary conditions (PBC). For this reason, this class of methods is not suitable for free boundary problems (free surfaces), where no additional conditions for the boundary atoms of the model's volume are imposed [65, 66]. In this case, other approaches should be used, such as MD.

QA simulations were eventually post-treated to accurately spot atom positions, and enhance the analysis of defect structures at the atomic scale. Indeed, the QA is intrinsically a continuous approach. At finite temperature, atoms are associated to atomic spheres with the fraton density function profile resembling a Gaussian. However, numerical fluctuations of the atomic density fields $\rho_\alpha(\boldsymbol{r}, t)$, as well as the emergence of partially delocalized, splitting, and coalescing atoms at interfaces (grain boundaries, fcc/bcc interface) and within the bulk (dislocation propagation) spices things up to accurately spot the center of atoms. While this behavior grants the method with its physical versatility and computational efficiency, it is a true hurdle when it comes to characterize defect structures. The `fratons2atoms` package [67] was harnessed using default parameters to interpret the structures from QA calculations and make an educated guess of the most reliable deterministic atomic structure associated to a given QA simulation. The `fratons2atoms` procedure and corresponding parameter setting are detailed in the Online Supplementary Material 3.

2. Numerical results: microstructure resulting from the fcc → bcc transformation

2.1. Fcc→bcc transformation at the microstructural level in the precipitate: formation of an internally twinned structure

Kinetic process of the fcc→bcc transformation. In this first section, the QA simulation of the full fcc→bcc transformation process from a small bcc nucleus embedded in the fcc precipitate into a complex bcc structure is prospected at the scale of the microstructure. In this regard, the different stages of the shape evolution and atomic structure of the bcc inclusion in the fcc parent phase within the precipitate (essentially made up of component 2 atoms) are displayed in figure 2. Therein, the Common Neighbor Analysis (CNA) from OVITO was used to visualize the microstructural evolution. Green color is for fcc (γ) structure, blue color for bcc (α), and red color for hcp structures. Any other crystallography is indicated in gray. This corresponds to perturbed (non crystalline) structures, including interfaces and boundaries. In detail, the full kinetic process is displayed in figure 2 (a) to (f), after cutting the simulation domain in the $(100)_\gamma$ plane. At initial state (figure 2 (a)), the precipitate consists in a small cubic bcc germ with V_1 KS OR (in blue), embedded in a fcc structure (in green). No coherency condition was imposed to the corresponding fcc/bcc interface (in gray) at initial time. However, the latter was observed to be achieved (or at least semi-coherency) after a few simulation steps. Moreover, the precipitate is itself (semi-) coherently embedded in the fcc matrix. To visualize the interface between the precipitate and the matrix (essentially containing component 1 atoms), a black dashed line was added as a guide for the eye at initial time, but also at $t = 500$ (figure 2 (b)) and $t = 750$ (figure 2 (c)).

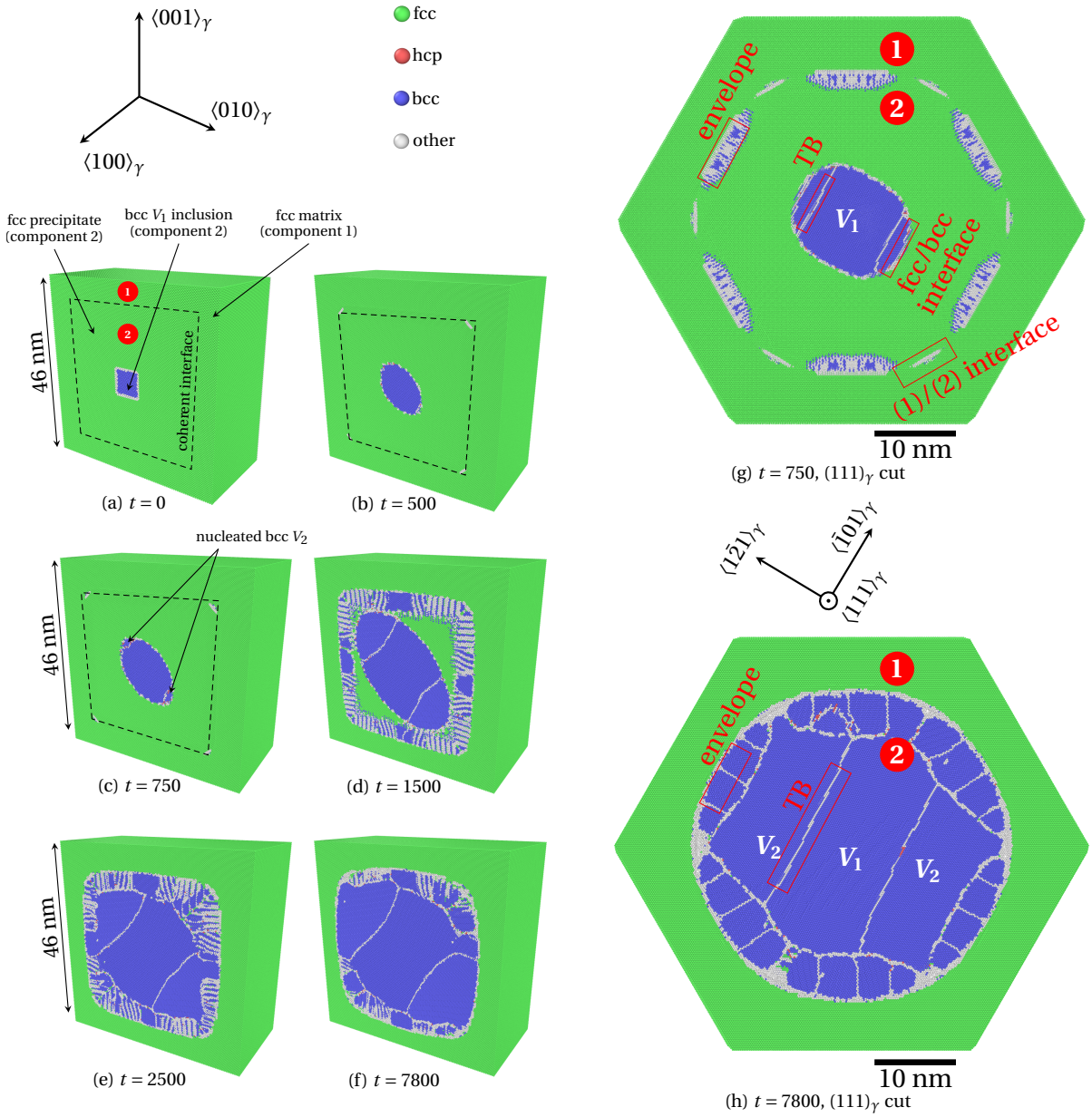

Figure 2: Kinetic evolution of the precipitate (mainly containing component 2 atoms)/ matrix (mainly containing component 1 atoms) structure, as simulated in the QA model on a 1024^3 simulation domain, using numerical parameters listed in table 1, starting from an initial bcc nucleus with KS OR (V_1). Visualization via the CNA of OVITO, after extraction of atom centers from the atomic density field ρ_2, using `fratons2atoms`. Green: fcc, blue: bcc, red: hcp and grey: unknown (perturbed structure). Components (1) and (2) are indicated by a circled 1 and 2 respectively. (a-f) Full kinetic process, cut in the $(100)_\gamma$ plane. (g-h) cut in the $(111)_\gamma$ plane at $t = 750$ (g) and $t = 7800$ (h). The precipitate and matrix are referred as (1) and (2) respectively. The twin boundary (TB), bcc envelope, fcc/bcc interface in the precipitate (1), and matrix (1)/precipitate (2) interface are indicated in red.

The bcc inclusion grows with a roughly ellipsoidal morphology flattened in a specific direction referred to as $\boldsymbol{n}_0$ from here, and estimated in the following. Based on Eshelby's theory of coherent inclusion [13, 68], a plate like morphology whose habit plane of normal vector $\boldsymbol{n}_0$ aligns with the invariant plane is prone to minimize the bulk strain energy of the inclusion. Along this line, the flattened direction $\boldsymbol{n}_0$ of the inclusion can be used as a first yardstick of the invariant plane direction normal. To estimate $\boldsymbol{n}_0$, the convex hull of the the bcc inclusion was calculated, and the least square ellipsoidal fitting of this surface was performed upon extending the constrained minimization method proposed in [69], from two to three dimensions. The convex hull of the bcc inclusion at $t = 1500$ is displayed in figure 3. It is equipped with the principal axis $\boldsymbol{x}_1$, $\boldsymbol{x}_2$ and $\boldsymbol{x}_3$ of the fitting ellipsoid, sorted in increasing order of ellipsoid parameter. It was found that $\boldsymbol{n}_0 \equiv \boldsymbol{x}_1 = \langle 0.56, 0.67, 0.49 \rangle$, which forks off the direction normal to the $(575)_\gamma$ plane by 3.8° only. The latter is a usual habit plane of a

martensite phase embedded in fcc austenite phase in many steels and iron based alloys [3, 6, 70, 71, 72, 73]. Besides, $\boldsymbol{x}_3$ corresponds to the largest ellipsoid parameter, and can thus be interpreted as the the preferential growth direction. It was found that $\boldsymbol{x}_3 = \langle 0.52, -0.74, 0.42 \rangle$, which draws relatively near to the $\langle 1\bar{2}1 \rangle_\gamma$ crystal orientation (7.57° deviation).

Regarding the shape of the bcc inclusion, it was mentioned in the model section that compared to iron based alloys, the lattice misfit between the fcc and bcc phases is underestimated in the present work (0.5 % vs. 2-4 %), while the yield between the bulk modulus is overestimated (1.4 vs. 1.27-1.35) [59, 60, 18]. This respectively leads to the underestimation of both the elastic strain energy and the relaxation energy contributions in the total elastic strain energy for a coherent inclusion [13]. The stress applied to the bcc inclusion is thus underestimated in the present work, resulting in a morphology of the inclusion less anisotropic than what could be expected experimentally, notably for the FeCuCo alloy.

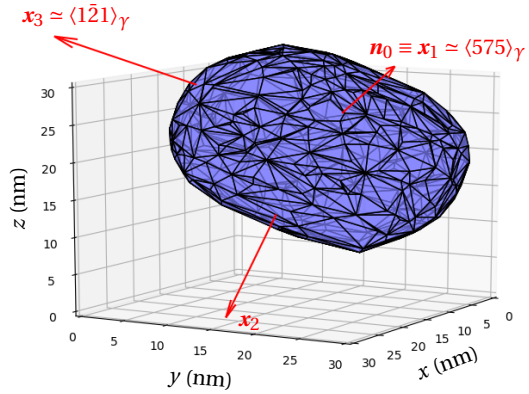

Figure 3: Convex hull of the bcc inclusion at $t = 1500$ and 3 principal axis $\boldsymbol{x}_1$ ($\sim$ invariant plane strain direction $\boldsymbol{n}_0$), $\boldsymbol{x}_2$ and $\boldsymbol{x}_3$ ($\sim$ preferential growth direction) of the fitting ellipsoid, sorted in increasing order of ellipsoid parameter.

As indicated in figure 2 (c), new structural domains siding the inclusion are formed after $t = 500$ (figure 2 (b)). A twin-like structure consisting in a series of three structural bcc domains with different orientations emerges therefrom. The orientation relationship between these structural domains is discussed in the following (see figure 4). As the bcc inclusion grows, a highly perturbed bcc envelope within the precipitate is nucleated at the precipitate/matrix interface (figures 2 (d-f)), due to the a significant strain in the vicinity of the precipitate/matrix interface. First, the growth of the bcc inclusion within the precipitate might induce a variation of the total volume of the precipitate, due to the lattice misfit between the fcc and bcc structures (see section 1.1). This strain is in turn be responsible for a substantial stress at the precipitate/matrix interface, thereby producing the heterogeneous nucleation of the bcc envelope. Second, the chemical repulsion between atoms of species (1) and (2) at the precipitate/matrix interface might also contribute to destabilize the fcc structure of the precipitate in this region. For $t > 1500$, the perturbed envelope organizes into numerous small bcc structure domains, as shown in figures 2 (e) and (f). At longer times, most structure domains coalesce, whilst the envelope itself starts to merge with the bcc inclusion ($t = 7800$). Then, the bcc inclusion grows within the fcc structure until the full fcc→bcc transformation is achieved in the precipitate. The transient ($t = 750$) and late stage ($t = 7800$) structures of the transforming precipitate are elucidated in the $(111)_\gamma$ plane in more details in figures 2 (g) and (h) respectively. In these figures, the position of the matrix an the precipitate are indicated by the index (1) and (2) respectively. The emerging bcc envelope, the fcc/bcc interface between within the precipitate, the twin boundaries (TB) between bcc structural domains of the inclusion, and the precipitate/matrix ((1)/(2)) interfaces are framed by a red rectangles. It should be noted that the analysis of the precipitate/matrix ((1)/(2)) interfaces was not carried out in this work.

Numerical diffraction analysis of the twinning structure. The identification of the crystallography of the structure domains within the inclusion was achieved via the diffraction analysis of the atomic configurations extracted from QA simulations. To that end, the diffraction intensity $I_2(\boldsymbol{k}) = \hat{\rho}_2(\boldsymbol{k}, t)\hat{\rho}_2^*(\boldsymbol{k}, t)$ of the component 2 atoms corresponding to the precipitate was calculated, where $\hat{\rho}_2^*$ refers to the complex conjugate of $\hat{\rho}_2$. The simulated diffraction pattern in the $(111)_\gamma$ plane at $t = 1500$ is presented in figure 4. Diffraction spots corresponding to three crystal structures can be observed. Each structure is identified by different color circles. Green circles single out the diffraction spots of the fcc structure, including $(\bar{2}02)_\gamma$ and $(0\bar{2}2)_\gamma$ points. Red circles enclose the diffraction spots of the bcc structure with KS OR V_1 (α_1 phase), such as $(2\bar{1}1)_{\alpha_1}$ and $(\bar{2}1\bar{1})_{\alpha_1}$. Finally, the diffraction spots emphasized by blue circles can be obtained by reflection of the diffraction pattern of the KS

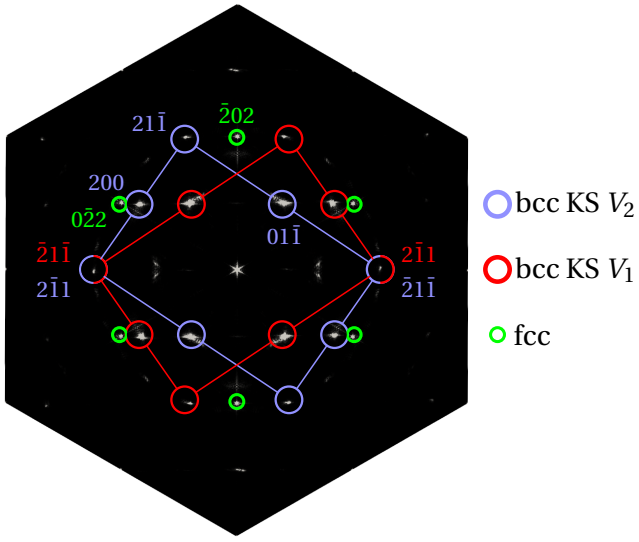

Figure 4: Diffraction pattern in the $(111)_\gamma$ plane, as obtained from the projection of the diffraction intensity $I_2(\boldsymbol{k})$ of the second component (precipitate). The diffraction spots corresponding to the bcc structure with KS OR V_1 are indicated in red, KS OR V_2 in blue, and fcc in green.

OR V_1 variant. The superimposition of two (blue) spots with the $(2\bar{1}1)_{\alpha_1}$ and $(\bar{2}1\bar{1})_{\alpha_1}$ (red) spots additionally indicates that the structure corresponding to the blue spots is the mirror image of the bcc structure with KS OR V_1 in the $(2\bar{1}1)_{\alpha_1}$ plane. This is the bcc structure with KS OR V_2. This structure will be referred to as α_2 in the following. Therefore, we deduce that the structure domains formed after $t = 750$ have the V_2 KS OR. The corresponding rotation matrix is provided in the Appendix B.

The formalism of deformation twinning [74] provides a convenient toolbox to characterize the present twinning structure. Based on the analysis of figure 4, the twinning plane is $K_1 = (2\bar{1}1)_{\alpha_1}$, and the shear plane is $P = (111)_\gamma \parallel (011)_{\alpha_1}$. The twinning direction can then be defined as the intersection line between the shear plane and the twinning plane, namely $\eta_1 = \langle\bar{1}\bar{1}1\rangle_{\alpha_1}$. The corresponding twinning mode is thus $(2\bar{1}1)_{\alpha_1}|\langle\bar{1}\bar{1}1\rangle_{\alpha_1}$. It is prevalent in various iron based alloys [75, 76]. In addition, it was found that the misorientation angle $\theta \simeq 69.5°$ between twinning variants V_1 and V_2 around the rotation axis $\langle 011\rangle_{\alpha_1}$ was consistent with the predicted value $\theta^{\text{id}} = 70.5°$. For this mode, twinning proceeds by homogeneous simple shear deformation of amplitude $s = 1/\sqrt{2}$, without shuffling. This deformation achieves perfect coincidence of lattices of both twins in the shear plane.

2.2. Atomic structure of twin boundaries (TB) and propagation mechanism based on the glide of partial twin dislocations

The twinned domains V_1 and V_2 envisioned in figure 2 are connected by twin boundaries (TB) lying parallel to the V_1/V_2 twinning plane $K_1 = (2\bar{1}1)_{\alpha_1}$. Two such TB are displayed in figure 5(a) and 5(b). Their location in the $(011)_{\alpha_1}$ plane is given by the row of gray atoms in OVITO's CNA (perturbed structure) which marks the transition from one bcc variant to another. The more accurate location of the TB along gray atoms can be further determined, depending on the type of TB (red dashes in figures 5(a) and 5(b)). In bcc systems, TB can be of two types: reflection (R) and isosceles (I) [77] as sketched in figure 6(a). In the first case (figure 6(a), left), the twinned structure is obtained by reflection in the twinning plane $(2\bar{1}1)_{\alpha_1}$, and the TB is precisely spotted at the reflection plane which cuts the center of gray atoms. In the second case (figure 6(a), right), the atoms belonging to one variant are translated by a vector $\boldsymbol{t}_I = \frac{1}{12}\langle\bar{1}\bar{1}1\rangle_{\alpha_1}$ compared to the reflection TB, and the mirror symmetry is violated. In that case, the TB is located between the $(2\bar{1}1)_{\alpha_1}$ twinning plane and the next $(2\bar{1}1)_{\alpha_1}$ plane.

In this work, we mostly observed isosceles (I) twin boundaries (figure 5(a) –top and bottom– and figure 5(b)). The isosceles nature of the top TB portion in figure 5(a) is demonstrated in figure 6(b) (right), where atoms belonging to variant V_2 (blue triangles) are superimposed to atoms belonging to variant V_1 (red squares) in the $(011)_{\alpha_1}$ plane, after $(2\bar{1}1)_{\alpha_1}$ plane reflection. As a result, atoms belonging to variants V_1 and V_2 are shifted along the $\langle\bar{1}\bar{1}1\rangle_{\alpha_1}$ direction by the translation vector $\boldsymbol{t}_I$. Portions of reflection (R) twin boundaries were also identified (strip of TB in the center of figure 5(a)). Using the same procedure as for the isosceles TB, figure 6(a) evidences the mirror symmetry between the two variants close to this portion of TB, insofar as atoms belonging to V_1 and V_2 superimpose after $(2\bar{1}1)_{\alpha_1}$ plane reflection.

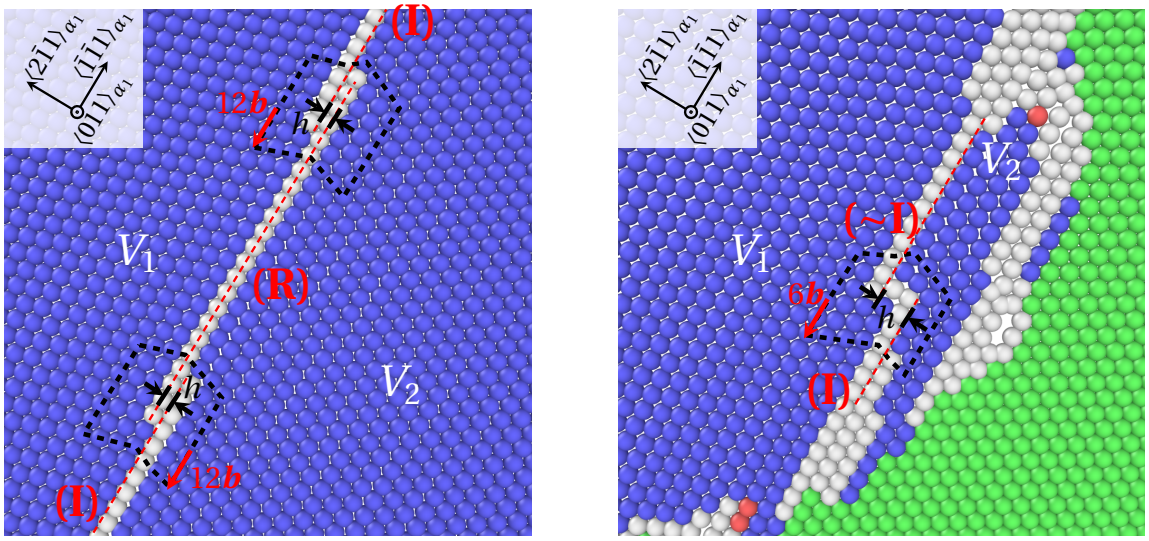

(a) IR+RI couple

(b) Z dislocation (1)

Figure 5: Twin dislocations analysis in the close packed plane $(111)_\gamma$ as extracted from QA simulations at $t = 1500$. (a) Partial twin dislocation couple (IR+RI) with step $h = a_2/(2\sqrt{6})$, Burgers vector $\boldsymbol{b} = \frac{1}{12}\langle \bar{1}\bar{1}1\rangle_{\alpha_1}$, connected by a strip of reflection TB (R). Elsewhere, the TB is isosceles (I). (b) Zonal twin dislocation (Z) with step $h = 2a_2/\sqrt{6}$, Burgers vector $\boldsymbol{b} = \frac{1}{6}\langle \bar{1}\bar{1}1\rangle_{\alpha_1}$. A video of partial twin dislocations motion can be found in the Online Supplementary Material.

During the propagation of TB, the transition from one type of TB to another –(I)→(R) and (R)→ (I)– is accompanied by the local re-stacking of $(2\bar{1}1)_{\alpha_1}$ planes, which results in the shift of the interface along the direction $\langle 2\bar{1}1\rangle_{\alpha_1}$ perpendicular to the twinning plane. In the present work, the amplitude of the shift was observed to be half the distance between two successive $(2\bar{1}1)_{\alpha_1}$ planes. This is materialized by the formation of a step with height $h = h_{IR/RI} = a_2/(2\sqrt{6})$, as indicated by the mismatch between red dashed lines indicating the TB in figure 5(a).

TB steps also bear a dislocation nature referred to as twinning dislocation [78, 79, 80, 74]. In figure 5(a), the two steps correspond to two partial twin dislocations (IR and RI). Each partial is framed by its Burgers circuit (black dashed line in figures 5(a) and 5(b)) traced out around the dislocation in the FS/RH reference crystal convention [80]. The calculated Burgers vector $\boldsymbol{b}$ is close to the theoretical partial IR twin dislocation: $\boldsymbol{b} \simeq \boldsymbol{b}_{\mathrm{IR/RI}} = \frac{1}{12}\langle \bar{1}\bar{1}1\rangle_{\alpha_1}$. The correspondence $\boldsymbol{b}_{\mathrm{IR/RI}} = \boldsymbol{t}_I$ indicates that (IR) and (RI) partial twin dislocations carry the translation of atoms close to the TB, when switching from (I) to (R) and (R) to (I) types of TB. Moreover, in the present simulations, the vast majority of partial twin dislocations form (IR+RI) pairs connected by a strip of reflection (R) interface, and bordered by two strips of isosceles (I) interface (figure 5(a)). From the general theory of twin dislocations [80, 74], we surmise that the two partial dislocations having the same Burgers vector repel one another, up to a distance where the increase of (R) type TB energy balances the repulsion between partials.

Regarding the dynamics of twin variant growth, we could observe that the propagation of the TB exclusively proceeds by the glide of pairs (IR+RI) of partial twin dislocations (see movies 1 and 2 of the Online Supplementary Material), which translates TB steps along the $\langle \bar{1}\bar{1}1\rangle_{\alpha_1}$ direction parallel to $\boldsymbol{b}_{\mathrm{IR/RI}}$. The strong glissility of partial twin dislocations which roots the propagation of the TB, stems from their wide core (diffuse step) (see figure 5(a)). As a matter of fact, it was shown in [81] that the double $\frac{1}{12}\langle \bar{1}\bar{1}1\rangle_{\alpha}$ dislocation glide was the prominent TB propagation in different metals, including bcc iron. A more detailed description of this twin partials glide process can also be found there.

Close to the fcc/bcc interface, zonal dislocations (Z) characterized by the Burgers vector $\boldsymbol{b}_{\mathrm{Z}} = \frac{1}{6}\langle \bar{1}\bar{1}1\rangle_{\alpha_1}$, and a step height of two $(2\bar{1}1)_{\alpha_1}$ interplanar spacing could seldom be observed, as displayed in figure 5(b). However, zonal dislocations are usually associated to a different twinning mode in bcc systems [82] than the present $(2\bar{1}1)_{\alpha_1}|\langle \bar{1}\bar{1}1\rangle_{\alpha_1}$ mode. The emergence of (Z) dislocations might thus be induced by the stress exerted by the fcc/bcc interface in the close vicinity. From the kinetic perspective, zonal dislocations are poorly glissile, and their contribution to TB propagation should thus be negligible.

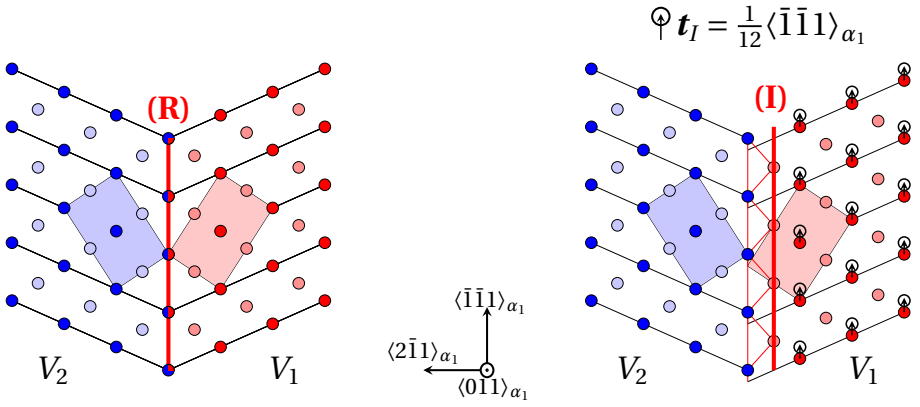

(a) (I) and (R) twin boundary (theory)

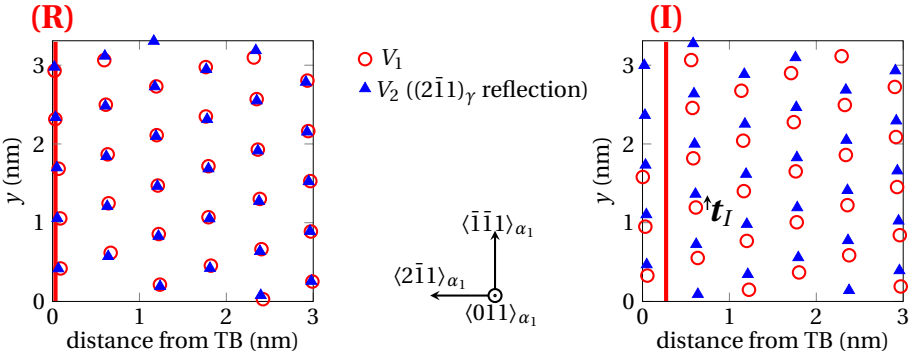

(b) (I) and (R) twin boundary (simulation)

Figure 6: Reflection (R) and isosceles (I) TB structure for the $(2\bar{1}1)_{\alpha_1}|\langle\bar{1}\bar{1}1\rangle_{\alpha_1}$ twinning mode, projected on the $(011)_\alpha$ plane. (I) TB obtained from (R) TB by imposing an additional translation of $\boldsymbol{t}_I = \langle\bar{1}\bar{1}1\rangle_{\alpha_1}$ at the interface. (a) Schematic representation. Dark blue: V_2 bcc atoms on the $(011)_\alpha$ plane. Dark red: V_1 bcc atoms in the $(011)_\alpha$ plane. Light blue: V_2 bcc atoms in the plane above and beneath the $(011)_\alpha$ plane. Light red: V_1 bcc atoms in the plane above and beneath the $(011)_\alpha$ plane. (b) TB as simulated by QA at $t = 1500$. Red circles: V_1 atoms in the $(011)_\alpha$ plane. Blue triangles: V_2 atoms in the $(011)_\alpha$ plane after $(1\bar{2}1)_\gamma$ plane reflection.

2.3. Atomic study of the fcc/bcc interface: defect structure and propagation mechanism via screw dislocations glide

Surface relief of the semi-coherent fcc/bcc interface. The bcc inclusion extracted from QA simulations at $t = 1500$ is presented in figure 7, using OVITO's visual rendering to magnify the surface relief. It was obtained by removing all atoms with fcc first neighbor environment, so that atoms labeled as bcc, hcp and perturbed structures were considered to belong to the inclusion in this figure.

The relief of the inclusion takes the form of a series of surface units consisting in $(111)_\gamma \parallel (011)_\alpha$ terraces, separated by $\langle\bar{1}01\rangle_\gamma$ steps of one or several $(111)_\gamma$ interplanar spacings. Three $(011)_\alpha \parallel (111)_\gamma$ planes taken on the top of the inclusion (top terrace) where the average orientation of the interface is close to the $(011)_\alpha$ plane are enlarged on the top right of figure 7. The corresponding terraces are flagged by transparent blue planes. The same is done for three terraces spotted more on the side of the inclusion (side terrace, at the bottom right of figure 7). From this, it appears that $(111)_\gamma$ terraces can be found all over the surface of the inclusion. However, the length of these terraces is bigger when the average orientation of the interface is close to the $(011)_\alpha$ terrace plane (top and bottom of the inclusion), and smaller otherwise (side of the inclusion).

In virtue of the TM [14], the fcc/bcc interface with KS OR should be fully coherent at $(011)_\alpha \parallel (111)_\gamma$ terraces. Under this hypothesis, the total misfit strain at the coherent $(011)_\alpha$ terrace can be expressed in the terrace plane coordinate frame $(\langle\bar{1}10\rangle_\gamma, \langle11\bar{2}\rangle_\gamma, \langle111\rangle_\gamma)$ as:

$$S_t = \begin{pmatrix} \epsilon^{\text{tot}}_{XX} & 0 & 0 \\ 0 & \epsilon^{\text{tot}}_{YY} & 0 \\ 0 & 0 & 0 \end{pmatrix}, \tag{10}$$

where both the deformation of the bcc and fcc phases are accounted for in the total strain. The infinitesimal strain introduced in equation 10 can conveniently be approximated using the fcc and bcc lattice parameters

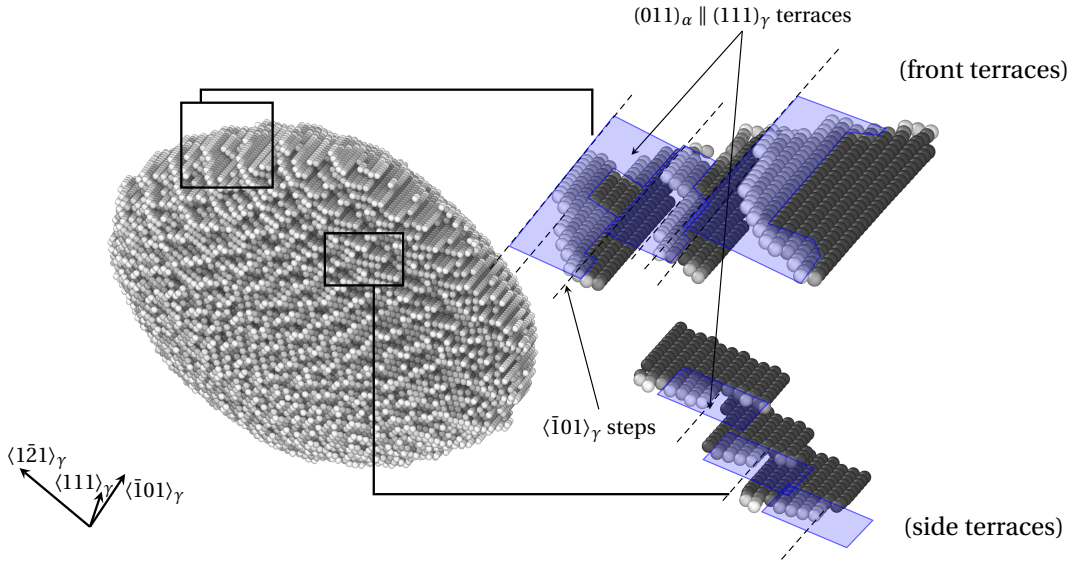

Figure 7: Surface relief of the bcc inclusion (bcc+unknown+hcp atoms as provided by OVITO CNA) as extracted from QA simulations at $t = 1500$, using OVITO's 'ambient occlusion' visual rendering. Top (top right) and side (bottom right) coherent units consisting in $(011)_\alpha \parallel (111)_\gamma$ terraces are spotted by transparent blue planes. Shades of gray reflect the distance of atoms from the fcc/bcc interface.

only. For that purpose, we introduce the interatomic distances d^α_{XX} and d^α_{YY} for the bcc structure, as well as d^γ_{XX} and d^γ_{YY} for the fcc structure, in the $\langle\bar{1}00\rangle_\alpha \parallel \langle\bar{1}10\rangle_\gamma$ and $\langle 11\bar{2}\rangle_\gamma \parallel \langle 01\bar{1}\rangle_\alpha$ directions. They respectively correspond to the small and large diagonal of the atomic rhombi depicted in figure 8(a). This rhombi delineates the atomic sites on the $(011)_\alpha \parallel (111)_\gamma$ planes for the unstrained fcc (green dashes) and bcc (blue line) structures and the coherent state (black line). In the present work, $a_1 = 8.0\Delta x = 0.36$ nm and $a_2 = 6.5\Delta x = 0.293$ nm, so that $d^\alpha_{XX} = a_2 = 0.293$ nm, $d^\alpha_{YY} = \sqrt{2}a_2 = 0.414$ nm, $d^\gamma_{XX} = \sqrt{2}/2a_1 = 0.255$ nm and $d^\gamma_{YY} = \sqrt{3/2}a_1 = 0.441$ nm.

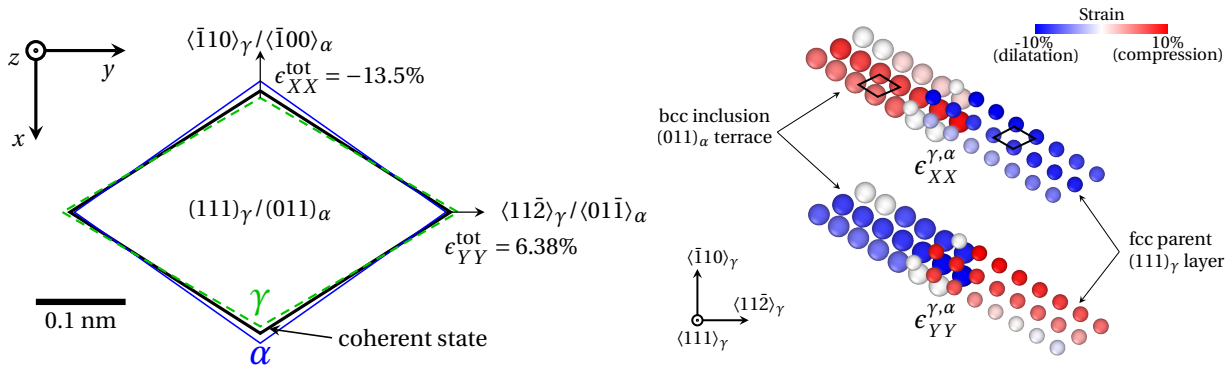

(a) Atomic rhombi (b) Strain (OVITO)

Figure 8: Misfit strain at the coherent $(011)_\alpha \parallel (111)_\gamma$ inclusion terrace expressed in the terrace plane coordinate frame $(\langle\bar{1}10\rangle_\gamma, \langle 11\bar{2}\rangle_\gamma, \langle 111\rangle_\gamma)$. (a) Scale drawing of the atomic rhombi in the terrace plane. Blue lines represent the unstrained bcc structure, green dashed lines the unstrained parent crystal, and bold black lines the coherent state. (b) QA calculation ($t = 1500$) at one $(011)_\alpha$ coherent terrace. Top: $\epsilon^{\gamma,\alpha}_{XX}$. Bottom: $\epsilon^{\gamma,\alpha}_{YY}$. In (b) the strain was calculated using OVITO (finite strain theory).

Then, keeping in mind that the infinitesimal strain in a given direction reflects the change in length over the initial length in this direction, $\epsilon^{\text{tot}}_{XX}$ can be approximated by the difference of interatomic distance between the fcc and bcc structures with respect to the average interatomic distance in the $\langle\bar{1}00\rangle_\alpha \parallel \langle\bar{1}10\rangle_\gamma$ (X) direction:

$$\epsilon^{\text{tot}}_{XX} \simeq 2(d^\gamma_{XX} - d^\alpha_{XX})/(d^\alpha_{XX} + d^\gamma_{XX}). \tag{11}$$

The same consideration applies for $\epsilon^{\text{tot}}_{YY}$ in the $\langle 11\bar{2}\rangle_\gamma \parallel \langle 01\bar{1}\rangle_\alpha$ (Y) direction:

$$\epsilon^{\text{tot}}_{YY} \simeq 2(d^\gamma_{YY} - d^\alpha_{YY})/(d^\alpha_{YY} + d^\gamma_{YY}). \tag{12}$$

This eventually gives $\epsilon_{XX}^{\text{tot}} \simeq -13.5\%$ and $\epsilon_{YY}^{\text{tot}} \simeq 6.38\%$ in the $(011)_\alpha \parallel (111)_\gamma$ terrace plane. Based on this preliminary calculation, a strong dilatation (compression) of the fcc (bcc) structure in the $\langle \bar{1}10\rangle_\gamma \parallel \langle \bar{1}00\rangle_\alpha$ (x) direction, and compression (dilatation) of the fcc (bcc) structure in the $\langle 11\bar{2}\rangle_\gamma \parallel \langle 01\bar{1}\rangle_\alpha$ (y) direction should be observed at coherent terraces.

To ascertain the coherency of $(011)_\alpha$ terraces in the present QA simulations, the deformation of the fcc and bcc structures with respect to the unstrained state were calculated at these terraces. For that purpose, the strain field was calculated using OVITO based on the finite strain theory in the fcc referential frame. Then, the obtained strain tensor was expressed in the terrace plane coordinate frame $(\langle \bar{1}10\rangle_\gamma, \langle 11\bar{2}\rangle_\gamma, \langle 111\rangle_\gamma)$. The two principal components XX and YY of the fcc and bcc strains as expressed in the terrace referential plane could then be displayed in figure 8(b) for $t = 1500$, wherein big spheres correspond to atoms with bcc environment and belonging to the $(011)_\alpha$ plane, and small spheres correspond to atoms with fcc environment and belonging to the interfacial $(011)_\alpha \parallel (111)_\gamma$ plane. The colormap reflects the amplitude of the accommodation strain for each phase. In the (x) direction, the bcc phase is strongly compressed while the fcc structure is dilated. In the (y) direction, it is the opposite situation (see figure 8(b)).

Identification and characterization of the dislocation network at the fcc/bcc interface. To understand the mechanism rooting the propagation of the fcc/bcc interface, the defect structure at this interface in the $(011)_\alpha \parallel (111)_\gamma$ plane is first prospected in figures 9 and 10. Therein, gray atoms indicate the interphase structure connecting the fcc and the bcc phases, and green and blue spheres refer to atoms in the fcc and bcc structure, respectively. $(011)_\alpha$ terraces are schematically delineated by terrace edges aligned with the $\langle \bar{1}01\rangle_\gamma$ direction (front edge at the top right in figure 7), and the $\langle 1\bar{1}0\rangle_\gamma / \langle 0\bar{1}1\rangle_\gamma$ directions (side edge at the bottom right in figure 7).

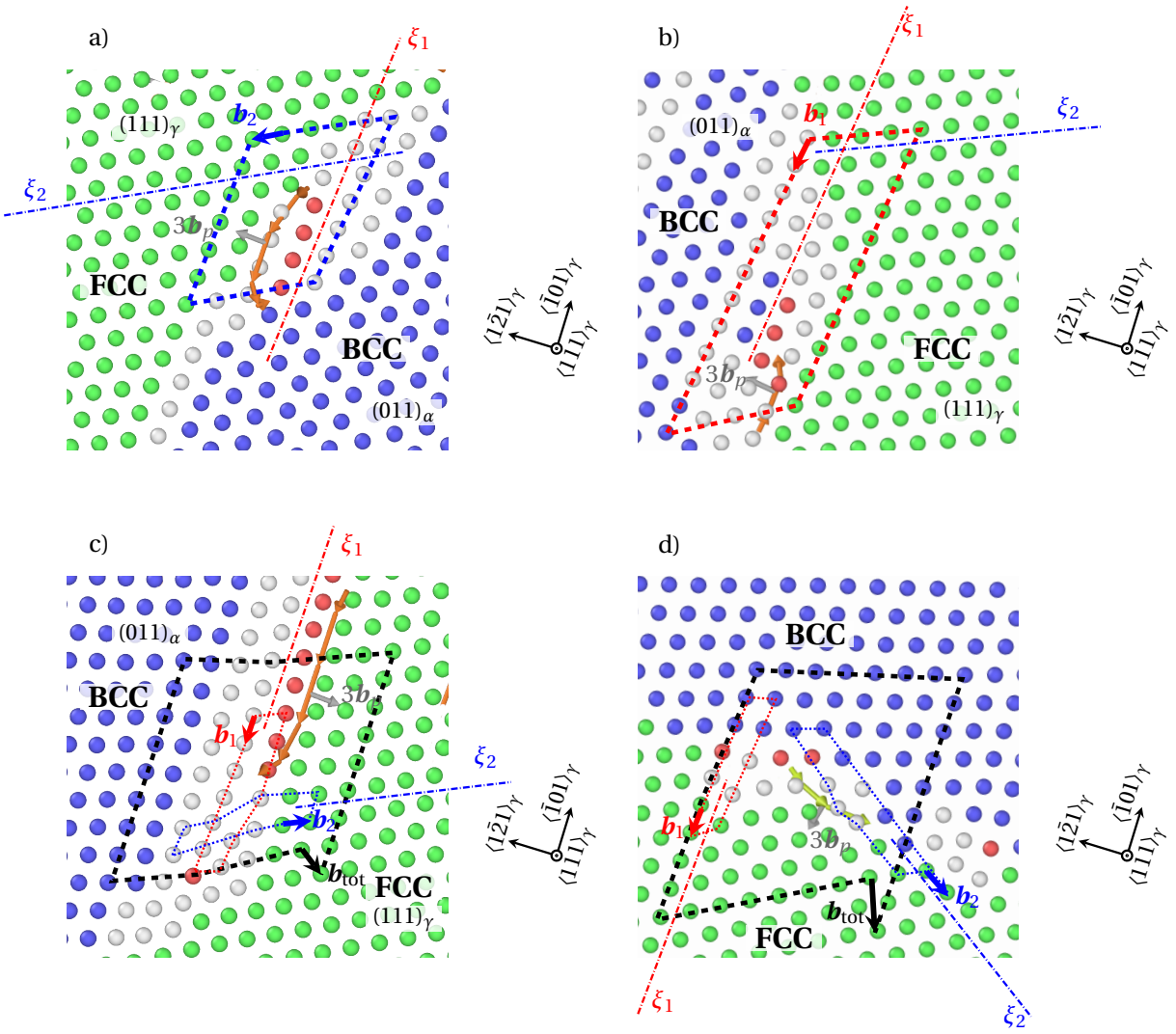

Figure 9: Defect structure of the fcc/bcc interface of $(011)_\alpha$ terraces, as extracted from QA simulations at $t = 750$. Visual rendering uses OVITO's CNA and Diffraction analysis in the fcc structure. 1/ Along front edge ($\langle\bar{1}01\rangle_\gamma$ direction): (fcc) stacking fault (SF) marked by $\langle\bar{1}01\rangle_\gamma$ rows of hcp atoms, bordered by Shockley partial dislocations (orange line) with Burgers vector $\boldsymbol{b}_p = \pm\frac{1}{6}\langle 1\bar{2}1\rangle_\gamma$ (gray arrow), and accompanied by fcc screw dislocation with Burgers vector $\boldsymbol{b}_1 = \pm\frac{1}{2}\langle\bar{1}01\rangle_\gamma$ (red arrow) and dislocation line $\xi_1 = \langle\bar{1}01\rangle_\gamma$ (red dash-dotted line). 2/ Along side edge ($\langle 1\bar{1}0\rangle_\gamma/\langle 0\bar{1}1\rangle_\gamma$ directions): (fcc) SF + Shockley partials (yellow tube) with $\boldsymbol{b}_p = \pm\frac{1}{6}\langle\bar{1}12\rangle_\gamma$ (gray arrow), siding fcc screw dislocation with $\boldsymbol{b}_2 = \pm\frac{1}{2}\langle 1\bar{1}0\rangle_\gamma$ and $\pm\frac{1}{2}\langle 0\bar{1}1\rangle_\gamma$ (blue arrow) and $\xi_2 = \langle\bar{1}01\rangle_\gamma/\langle 0\bar{1}1\rangle_\gamma$ (blue dash-dotted line). a) Burgers circuit for $\boldsymbol{b}_2$ dislocations only (blue dashed line). b) Burgers circuit for $\boldsymbol{b}_1$ dislocations only (red dashed line). c) and d) Burgers circuit for resulting dislocation $\boldsymbol{b}_{\rm tot}$ (black dashed line), and Burgers circuit for $\boldsymbol{b}_2$ and $\boldsymbol{b}_1$ contributions (blue and red dotted line).

At front edges ($\langle\bar{1}01\rangle_\gamma$ direction), $\langle\bar{1}01\rangle_\gamma$ rows of atoms belonging to the hcp phase (in red) indicate the presence of $\langle\bar{1}01\rangle_\gamma$ stacking faults [18] produced by Shockley partial edge dislocations (orange tube) with Burgers vector $\boldsymbol{b}_p = \pm\frac{1}{6}\langle 1\bar{2}1\rangle_\gamma$ (gray arrow). The $\langle\bar{1}01\rangle_\gamma$ SF+$\frac{1}{6}\langle 1\bar{2}1\rangle_\gamma$ partial set is accompanied by a fcc screw dislocation with the Burgers vector $\boldsymbol{b}_1 = \frac{1}{2}\langle\bar{1}01\rangle_\gamma$ (red arrow) and the dislocation line $\xi_1 = \langle\bar{1}01\rangle_\gamma$ (red dashdotted line). One $\boldsymbol{b}_1$ dislocation is singled out in figure 9 b), where it is circumscribed by its Burgers circuit (red dashed line).

A similar structure is found at side edges ($\langle 1\bar{1}0\rangle_\gamma/\langle 0\bar{1}1\rangle_\gamma$ directions). Therein, Shockley partial edge dislocations (yellow tube) with Burgers vector $\boldsymbol{b}_p = \pm\frac{1}{6}\langle\bar{1}12\rangle_\gamma$ produce $\langle 1\bar{1}0\rangle_\gamma/\langle 0\bar{1}1\rangle_\gamma$ SF. This set of defects is again tied to a second class of fcc screw dislocations having the Burgers vector $\boldsymbol{b}_2 = \pm\frac{1}{2}\langle 1\bar{1}0\rangle_\gamma/\pm\frac{1}{2}\langle 0\bar{1}1\rangle_\gamma$ (blue arrow) and the dislocation line $\xi_2 = \langle\bar{1}01\rangle_\gamma/\langle 0\bar{1}1\rangle_\gamma$ (blue dashdotted line). One $\boldsymbol{b}_2$ dislocation is isolated in figure 9 a), where it is framed by its Burgers circuit (blue dashed line).

The net Burgers vector $\boldsymbol{b}_{\rm tot}$ (black arrow) of $\boldsymbol{b}_1$ and $\boldsymbol{b}_2$ dislocations is defined in figure 9 c) and 9 d) by the closure failure of the Burgers circuit (black dashed line) which encompasses both $\boldsymbol{b}_1$ and $\boldsymbol{b}_2$ dislocations as circumscribed by their own Burgers circuits (blue and red dotted lines). The presence of similar screw dislocations at the fcc/bcc interface in Fe-0.6C-2Si-1Mn and Fe-20Ni-5.5Mn steels was reported in [2].

Furthermore, $\boldsymbol{b}_2$ dislocations contribute to accommodate the misfit between the fcc structure in the $\langle 01\bar{1}\rangle_\gamma$

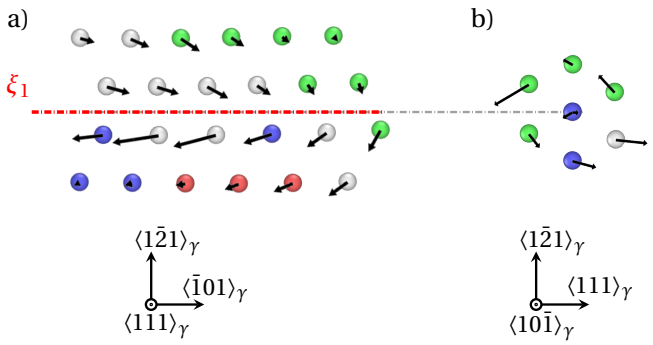

Figure 10: $\boldsymbol{b}_1$ screw dislocation at the fcc/bcc interface step of $(011)_\alpha$ terraces, as extracted from QA simulations at $t = 800$. Visual rendering uses OVITO's CNA. Black arrows represent the displacement field (amplitude $\times 50$) of atoms, between close times $t = 800$ and $t = 802.5$. (a) ξ_1 dislocation line (red dashed line) in the $(011)_\alpha \parallel (111)_\gamma$ plane. b) $(\bar{1}01)_\gamma$ plane slice of the step, aligned with (a). Two videos of a screw dislocation glide in the $(111)_\gamma$ and $(10\bar{1})_\gamma$ planes corresponding to a) and b) respectively can be found in the Online Supplementary Material.

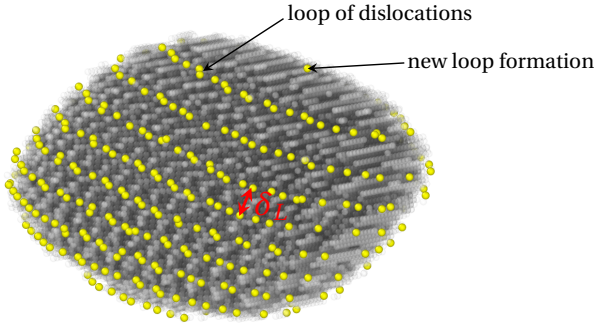

Figure 11: 3D distribution of $\boldsymbol{b}_2$ dislocation cores (yellow spheres) at the interface of the inclusion (transparent gray atoms with ambient occlusion) as obtained by QA simulations at $t = 750$.

direction and the bcc structure in the $\langle 1\bar{1}1\rangle_\alpha$ (quasi-) parallel direction, for a curved fcc/bcc interface. One argument for that can be found in the three dimensional distribution of $\boldsymbol{b}_2$ dislocation cores (yellow spheres) on the surface of the ellipsoidal inclusion in figure 11. These are distributed in lines of dislocation cores organized in loops which encircle the bcc inclusion, and lie in periodically distributed parallel planes. This type of defects was previously envisioned using a mixed MD-MC approach at the semi-coherent interface of bcc-Cr precipitates in a fcc-Cu matrix, where it was referred to as "dislocation loops" [33]. This periodicity can be related to the elastic accommodation of a twinned bcc particle with the fcc matrix. As was discussed in [83], the period Λ of the twinned interface is the ratio between the conventional surface energy γ_{TB} of the twin boundaries between two orientation variants, and the elastic energy E_{sc} related to the semicoherent interface:

$$\Lambda = \sqrt{\frac{\gamma_{\mathrm{TB}}}{\mu E_{\mathrm{sc}}} D}, \tag{13}$$

where D is the width of the plate, and μ is the shear modulus. In the present work, the periodic structure in figure 11 with period $\delta L = 1.36$ nm can be also related to the ratio between the energy of staking faults and the elastic energy. Herein, the increase of the elastic energy or the decrease of the staking faults energy will result in the increase of δL.

Fundamental mechanism for the propagation of the fcc/bcc interface and the fcc → bcc transformation. Based on these observations, the structure and propagation mechanism of the fcc/bcc interface in the case of an ellipsoidal bcc inclusion is schematized in figure 12, using the same color coding for dislocations as in figure 9.

At both front and side edges, we suggest that the fcc→bcc phase transition should follow the fcc→hcp→bcc transformation path. It is triggered by $\boldsymbol{b}_p$ Shockley partial dislocations that produce SF along the edge, where the fcc/bcc interface can be spotted. This path can be divided into two steps: first, a Shockley partial dislocation with Burgers vector $\frac{1}{6}\langle 1\bar{2}1\rangle_\gamma$ produces a SF which transforms the ABCABC stacking sequence of close-packed $(111)_\gamma$ planes of the fcc structure into the ABAB stacking sequence in the hcp phase. Then, the homogeneous deformation of the hcp structure produces the final transformation from $(111)_\gamma$ fcc to $(011)_\alpha$ bcc planes. This homogeneous deformation is carried by the glide of $\boldsymbol{b}_1$ and $\boldsymbol{b}_2$ fcc screw dislocations along there respective dislocation line. In detail, the glide generates a shear displacement of atomic positions along the edge in the $(011)_\alpha \parallel (111)_\gamma$ plane (figure 10 a)), while the rotation of atoms around the dislocation line (figure 10 b)) aligns the fcc perturbed structure on the bcc structure, in the vicinity of the step. The present mechanism provides an athermal/glissile propagation mode for a curved fcc/bcc interface [18].

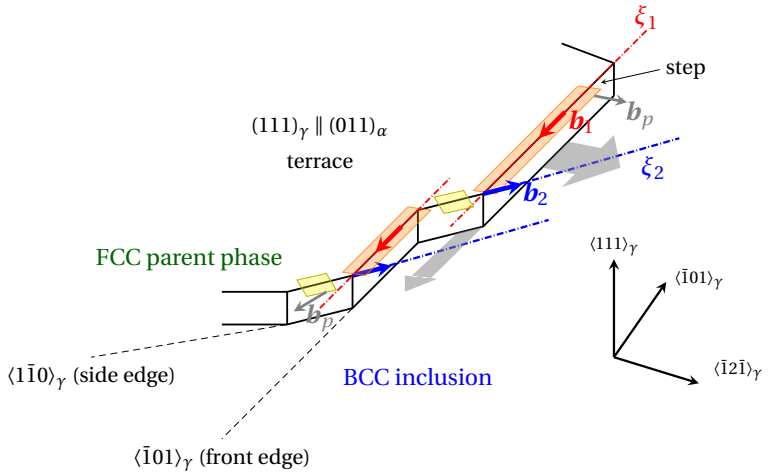

Figure 12: Schematic representation of fcc/bcc interface structure and propagation mechanism in the case of an ellipsoidal bcc inclusion. One $(011)_\alpha$ terrace consisting in $\langle \bar{1}01\rangle_\gamma$ and $\langle 1\bar{1}0\rangle_\gamma/\langle 0\bar{1}1\rangle_\gamma$ step edges and corners is depicted. The fcc→bcc interface is located at fcc SF (along $\langle \bar{1}01\rangle_\gamma$ in red, and $\langle 1\bar{1}0\rangle_\gamma/\langle 0\bar{1}1\rangle_\gamma$ in yellow) produced by fcc Shockley partial edge dislocations with Burgers vector $\boldsymbol{b}_p$. The terrace step propagates outward (gray arrows), by means of the glide of $\boldsymbol{b}_1$ (red arrow) screw dislocation along $\langle \bar{1}01\rangle_\gamma$ and $\boldsymbol{b}_2$ (blue arrow) screw dislocation along $\langle 1\bar{1}0\rangle_\gamma/\langle 0\bar{1}1\rangle_\gamma$.

3. Comparison with experimental results in a Fe-Cu alloy

To compare our predictions with a real system, the Cu-Fe alloys seems appropriate (see section 1.1). In this immiscible system, the nanosized Fe-rich particles precipitate in the Cu-rich matrix during the cooling stage of the casting process. The crystallographic features of the Fe-rich nanoparticle in the Cu-2.0Fe-0.5Co (wt. %) alloy was investigated via transmission electron microscopy (TEM). Details about experimental conditions are provided in the Appendix C. In figure 13 (a-c), a spherical Fe-rich nanoparticle is characterized by high resolution TEM (HRTEM) micrographs and Fast Fourier Transform (FFT) patterns along the $\langle 111\rangle_\alpha$ zone axis (ZA), indicating a bcc structure of Fe-rich nanoparticle and its KS OR with the fcc Cu matrix. Along the $\langle \bar{1}13\rangle_\alpha$ ZA of the same Fe-rich nanoparticle, a bcc twinned domains within the nanoparticle is displayed. It is accompanied by HRTEM exhibition and FFT pattern indexation (figure 13 (d-f). The amplified image of the twin boundary zone in figure 13 f) presents partial twin dislocation couple (IR+RI) corresponding to the numerical atomic structure displayed in figure 5 a). In addition, the FFT pattern of one Fe-rich nanoparticle along the $\langle 011\rangle_\alpha$ ZA indicates that twinning domains are formed with the KS OR variants V_1 and V_2 (figure 13 (g-i)). This is similar to the present QA simulations (figures 2 and 4). The theoretical misorientation angle between the KS variants V_1 and V_2 observed experimentally (70.62°, measured using e-Ruler 1.0) in figure 13 i) is also very close to the numerical value (70.5°). The experimental thickness of twin domains is avg. 8.0 nm (ranging from 2.2 to 23.6 nm) vs. 15 nm in simulations. This disparity stems from the fact that the simulation box in our simulations is smaller than the size of Fe-rich particle observed experimentally. However, it is shown in this study that this type of structures can be also observed in smaller particles using scaling parameters. It is also noteworthy that a bcc envelope emerges between one spheroidal bcc (iron) precipitate and the fcc (copper) matrix in figure 13 a) and d). We suggest that it might correspond to the transient envelope obtained in simulations (figure 2) between the bcc inclusion and the fcc parent phase.

As a conclusion, while a fully quantitative comparison between our experimental and modeling results is still beyond reach, it appears that the present numerical model finely reproduces the main characteristics of the

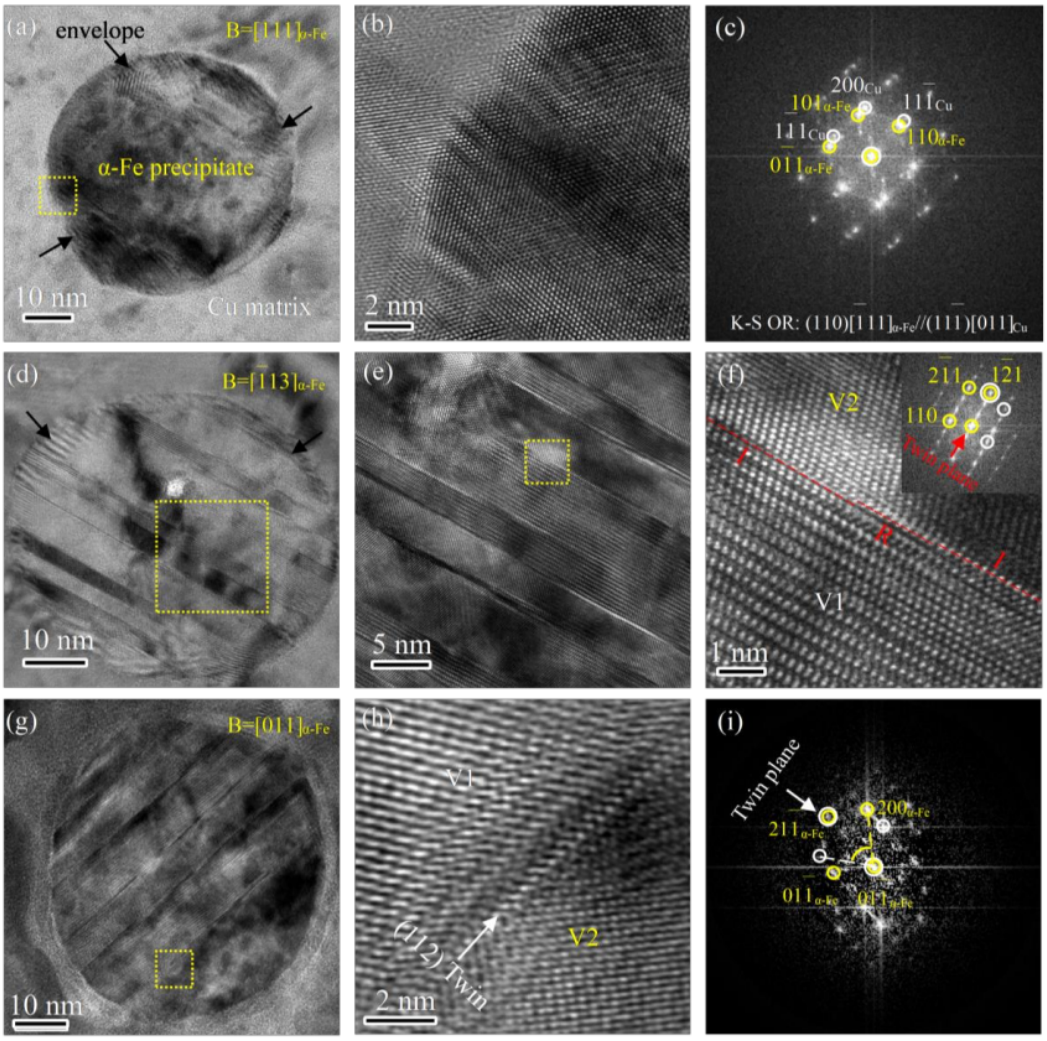

Figure 13: HRTEM analysis of one spherical iron-rich nanoparticle along different directions. a) HRTEM micrograph along $\langle 111\rangle_\alpha$ zone axis. b) Enlarged figure of dashed squire zone in a). c) FFT pattern corresponding to b), presenting the KS OR between the iron-rich nanoparticle and the copper matrix. d) HRTEM micrograph along $\langle \bar{1}13\rangle_\alpha$ zone axis, showing twinning domains. e) Enlarged figure of dashed squire zone in d). f) Zoom on the one of the twin boundaries marked by dashed squire zone in e) with partial twin dislocation couple (IR+RI), the inset showing its corresponding FFT pattern. Envelopes of the iron-rich nanoparticle were marked by black arrows in (a, d). g) HRTEM micrograph along $\langle 011\rangle_\alpha$ zone axis. h) Amplified figure of dashed squire zone in g). i) Corresponding FFT pattern of h), presenting the KS OR V_2 (yellow), and the KS OR V_1 (White).

fcc→bcc transformation in a precipitate/matrix binary system.

Conclusion

In this work, the QA was further developed to simulate the fcc→bcc transformation in a model binary system. For that purpose, it was equipped with new interaction potentials, and an original post-treatment procedure which allowed to analyze structural defects. At the microstructural scale, the bcc inclusion was found to grow from a bcc nucleus with KS OR, in the shape of a slightly flattened ellipsoid. An effective habit plane close to $(575)_\gamma$ which minimizes the bulk strain energy of the inclusion was determined as the plane normal to the flattened direction. Besides, the growth of the inclusion was accompanied by the spontaneous appearance of the second KS variant with twin related OR. The simulated diffraction pattern was used to identify the nature of this second variant and to determine the twinning plane and twinning direction. It was shown that the corresponding twinning mode is $(2\bar{1}1)_\alpha|\langle\bar{1}\bar{1}1\rangle_\alpha$. At the atomic level, twin boundaries were first found to be mostly of isosceles nature, albeit hosting strips of reflection boundaries between pairs of partial twin dislocations gliding along direction $\langle\bar{1}\bar{1}1\rangle_\alpha$. We concluded that the prominent mechanism of twin growth was the glide of dissociated $\langle\bar{1}\bar{1}1\rangle_\alpha$ twin dislocations along twin boundaries. Another feature predicted from our simulation is that the fcc/bcc interface of the bcc inclusion within the precipitate was found to consist in

$(111)_\gamma$ coherent terraces delineated by steps. Besides, the defect structure of terrace steps consists in pairs of $\frac{1}{2}\langle\bar{1}01\rangle_\gamma$ and $\frac{1}{2}\langle1\bar{1}0\rangle_\gamma$ fcc screw dislocations. Therefore, we could posit that the fcc/bcc interface athermal propagation was mainly carried by the glide of $\frac{1}{2}\langle\bar{1}0\bar{1}\rangle_\gamma$ screw dislocations along $\langle\bar{1}01\rangle_\gamma$ step edges, striding the fcc→hcp→bcc transformation path. Meanwhile, $\frac{1}{2}\langle1\bar{1}0\rangle_\gamma$ dislocations were assumed to accommodate the misfit between the fcc and bcc structures in the $\langle01\bar{1}\rangle_\gamma$ and $\langle1\bar{1}1\rangle_\alpha$ directions respectively. Finally, a first comparison with HRTEM observations of twinned iron rich precipitates in a cast Fe-Cu alloy proved qualitatively consistent with the present simulations.

As a conclusion, the present work demonstrates the potential of the QA, which belongs to the phase-field framework, to address the challenging issue of martensitic transformation, which is notoriously difficult to prospect experimentally. We thus suggest that the QA could be added to the existing numerical toolkit for fcc→bcc transformations, as on the one hand it is able to provide an atomistic description of the process, which usual coarse grained models such as the standard PFM cannot, while having the capacity to prospect such transformations on large spatial scales and for complex geometries, which remains challenging for usual atomistic approaches such as MD.

DATA AVAILABILITY

All datasets generated in the current study are available from the corresponding authors upon reasonable request.

References

[1] GB Olson and Morris Cohen. A general mechanism of martensitic nucleation: Part ii. fcc → bcc and other martensitic transformations. *Metallurgical transactions A*, 7(12):1905–1914, 1976.

[2] T Moritani, N Miyajima, T Furuhara, and T Maki. Comparison of interphase boundary structure between bainite and martensite in steel. *Scripta materialia*, 47(3):193–199, 2002.

[3] BPJ Sandvik and CM Wayman. Characteristics of lath martensite: Part ii. the martensite-austenite interface. *Metallurgical Transactions A*, 14(4):823–834, 1983.

[4] BPJ Sandvik and CM Wayman. Characteristics of lath martensite: Part iii. some theoretical considerations. *Metallurgical Transactions A*, 14(4):835–844, 1983.

[5] PM Kelly, A Jostsons, and RG Blake. The orientation relationship between lath martensite and austenite in low carbon, low alloy steels. *Acta Metallurgica et Materialia*, 38(6):1075–1081, 1990.

[6] Liang Qi, AG Khachaturyan, and JW Morris Jr. The microstructure of dislocated martensitic steel: Theory. *Acta materialia*, 76:23–39, 2014.

[7] X Ma and RC Pond. Parent–martensite interface structure in ferrous systems. *Journal of nuclear materials*, 361(2-3):313–321, 2007.

[8] C Bos, J Sietsma, and BJ Thijsse. Molecular dynamics simulation of interface dynamics during the fcc-bcc transformation of a martensitic nature. *Physical Review B*, 73(10):104117, 2006.

[9] Xiaoqin Ou, Jilt Sietsma, and Maria Jesus Santofimia. Molecular dynamics simulations of the mechanisms controlling the propagation of bcc/fcc semi-coherent interfaces in iron. *Modelling and Simulation in Materials Science and Engineering*, 24(5):055019, 2016.

[10] Monroe S Wechsler, DS Lieberman, and TA Read. On the theory of the formation of martensite. *Trans. Aime*, 197(11):1503–1515, 1953.

[11] JS Bowles and JK Mackenzie. The crystallography of martensite transformations i. *Acta metallurgica*, 2(1):129–137, 1954.

[12] CM á Wayman. Introduction to the crystallography of martensite transformations, 1964.

[13] Armen G Khachaturyan. *Theory of structural transformations in solids*. Courier Corporation, 2013.

[14] RC Pond, S Celotto, and JP Hirth. A comparison of the phenomenological theory of martensitic transformations with a model based on interfacial defects. *Acta materialia*, 51(18):5385–5398, 2003.

[15] JP Hirth and RC Pond. Compatibility and accommodation in displacive phase transformations. *Progress in Materials Science*, 56(6):586–636, 2011.

[16] JP Hirth. Dislocations, steps and disconnections at interfaces. *Journal of Physics and Chemistry of Solids*, 55(10):985–989, 1994.

[17] JP Hirth, J Wang, and CN Tomé. Disconnections and other defects associated with twin interfaces. *Progress in Materials Science*, 83:417–471, 2016.

[18] F Maresca and WA Curtin. The austenite/lath martensite interface in steels: Structure, athermal motion, and in-situ transformation strain revealed by simulation and theory. *Acta Materialia*, 134:302–323, 2017.

[19] Long-Qing Chen. Phase-field models for microstructure evolution. *Annual review of materials research*, 32(1):113–140, 2002.

[20] W Zhang, YM Jin, and AG Khachaturyan. Phase field microelasticity modeling of heterogeneous nucleation and growth in martensitic alloys. *Acta Materialia*, 55(2):565–574, 2007.

[21] Mahmood Mamivand, Mohsen Asle Zaeem, and Haitham El Kadiri. A review on phase field modeling of martensitic phase transformation. *Computational Materials Science*, 77:304–311, 2013.

[22] H Song and JJ Hoyt. An atomistic simulation study of the migration of an austenite–ferrite interface in pure Fe. *Acta materialia*, 61(4):1189–1196, 2013.

[23] Teresa Castán and Per-Anker Lindgård. Kinetics of domain growth, theory, and monte carlo simulations: A two-dimensional martensitic phase transition model system. *Physical Review B*, 40(7):5069, 1989.

[24] Ying Chen and Christopher A Schuh. A coupled kinetic monte carlo–finite element mesoscale model for thermoelastic martensitic phase transformations in shape memory alloys. *Acta Materialia*, 83:431–447, 2015.

[25] X Ou. Molecular dynamics simulations of fcc-to-bcc transformation in pure iron: A review. *Materials Science and Technology*, 33(7):822–835, 2017.
[26] H Song and JJ Hoyt. A molecular dynamics simulation study of the velocities, mobility and activation energy of an austenite–ferrite interface in pure Fe. *Acta materialia*, 60(10):4328–4335, 2012.
[27] Ju Li, Sanket Sarkar, William T Cox, Thomas J Lenosky, Erik Bitzek, and Yunzhi Wang. Diffusive molecular dynamics and its application to nanoindentation and sintering. *Physical Review B*, 84(5):054103, 2011.
[28] RA Johnson and DJ Oh. Analytic embedded atom method model for bcc metals. *Journal of Materials Research*, 4(5):1195–1201, 1989.
[29] GJ Ackland, DJ Bacon, AF Calder, and T Harry. Computer simulation of point defect properties in dilute Fe-Cu alloy using a many-body interatomic potential. *Philosophical Magazine A*, 75(3):713–732, 1997.
[30] R Meyer and P Entel. Martensite-austenite transition and phonon dispersion curves of Fe_{1-x} Ni_x studied by molecular-dynamics simulations. *Physical Review B*, 57(9):5140, 1998.
[31] C Bos, F Sommer, and EJ Mittemeijer. A kinetic monte carlo method for the simulation of massive phase transformations. *Acta materialia*, 52(12):3545–3554, 2004.
[32] H Song and JJ Hoyt. An atomistic simulation study of the crystallographic orientation relationships during the austenite to ferrite transformation in pure fe. *Modelling and Simulation in Materials Science and Engineering*, 23(8):085012, 2015.
[33] Fu-Zhi Dai, Zhi-Peng Sun, and Wen-Zheng Zhang. From coherent to semicoherent—evolution of precipitation crystallography in an fcc/bcc system. *Acta Materialia*, 186:124–132, 2020.
[34] Nikolas Provatas and Ken Elder. *Phase-field methods in materials science and engineering*. John Wiley & Sons, 2011.
[35] KR Elder, Mark Katakowski, Mikko Haataja, and Martin Grant. Modeling elasticity in crystal growth. *Physical review letters*, 88(24):245701, 2002.
[36] KR Elder and Martin Grant. Modeling elastic and plastic deformations in nonequilibrium processing using phase field crystals. *Physical Review E*, 70(5):051605, 2004.
[37] Ken R Elder, Nikolas Provatas, Joel Berry, Peter Stefanovic, and Martin Grant. Phase-field crystal modeling and classical density functional theory of freezing. *Physical Review B*, 75(6):064107, 2007.
[38] Michael Greenwood, Nana Ofori-Opoku, Jörg Rottler, and Nikolas Provatas. Modeling structural transformations in binary alloys with phase field crystals. *Physical Review B*, 84(6):064104, 2011.
[39] Nathan Smith and Nikolas Provatas. Generalization of the binary structural phase field crystal model. *Physical Review Materials*, 1(5):053407, 2017.
[40] Joel Berry, Jörg Rottler, Chad W Sinclair, and Nikolas Provatas. Atomistic study of diffusion-mediated plasticity and creep using phase field crystal methods. *Physical Review B*, 92(13):134103, 2015.
[41] Nana Ofori-Opoku, Vahid Fallah, Michael Greenwood, Shahrzad Esmaeili, and Nikolas Provatas. Multicomponent phase-field crystal model for structural transformations in metal alloys. *Physical Review B*, 87(13):134105, 2013.
[42] Matthew J Frick, Nana Ofori-Opoku, and Nikolas Provatas. Incorporating density jumps and species-conserving dynamics in xpfc binary alloys. *arXiv preprint arXiv:2005.09049*, 2020.
[43] KR Elder, Zhi-Feng Huang, and Nikolas Provatas. Amplitude expansion of the binary phase-field-crystal model. *Physical Review E*, 81(1):011602, 2010.
[44] Eli Alster, KR Elder, Jeffrey J Hoyt, and Peter W Voorhees. Phase-field-crystal model for ordered crystals. *Physical Review E*, 95(2):022105, 2017.
[45] Xiaofeng Yang and Daozhi Han. Linearly first-and second-order, unconditionally energy stable schemes for the phase field crystal model. *Journal of Computational Physics*, 330:1116–1134, 2017.
[46] Vidar Skogvoll, Audun Skaugen, Luiza Angheluta, and Jorge Viñals. Dislocation nucleation in the phase-field crystal model. *Physical Review B*, 103(1):014107, 2021.
[47] Mykola Lavrskyi, Helena Zapolsky, and Armen G Khachaturyan. Quasiparticle approach to diffusional atomic scale self-assembly of complex structures: from disorder to complex crystals and double-helix polymers. *Npj Computational Materials*, 2(1):1–9, 2016.
[48] H Zapolsky, G Demange, and Rafal Abdank-Kozubski. From the atomistic to the mesoscopic scale modeling of phase transition in solids. In *Diffusion Foundations*, volume 12, pages 111–126. Trans Tech Publ, 2017.
[49] O Kapikranian, H Zapolsky, Ch Domain, Renaud Patte, Cristelle Pareige, B Radiguet, and Philippe Pareige. Atomic structure of grain boundaries in iron modeled using the atomic density function. *Physical Review B*, 89(1):014111, 2014.
[50] O Kapikranian, H Zapolsky, R Patte, C Pareige, B Radiguet, and Philippe Pareige. Point defect absorption by grain boundaries in α-iron by atomic density function modeling. *Physical Review B*, 92(22):224106, 2015.
[51] N Mavrikakis, C Detlefs, PK Cook, M Kutsal, APC Campos, M Gauvin, PR Calvillo, W Saikaly, R Hubert, Henning Friis Poulsen, et al. A multi-scale study of the interaction of sn solutes with dislocations during static recovery in α-fe. *Acta Materialia*, 174:92–104, 2019.
[52] KX Chen, Pavel A Korzhavyi, G Demange, H Zapolsky, Renaud Patte, Julien Boisse, and ZD Wang. Morphological instability of iron-rich precipitates in cufeco alloys. *To be published*, 2020.
[53] AG Khachaturian. Ordering in substitutional and interstitial solid solutions. *Progress in Materials Science*, 22(1-2):1–150, 1978.
[54] Bence Gajdics, János J Tomán, Helena Zapolsky, Zoltán Erdélyi, and Gilles Demange. A multiscale procedure based on the stochastic kinetic mean field and the phase-field models for coarsening. *Journal of Applied Physics*, 126(6):065106, 2019.
[55] Bence Gajdics, János J Tomán, and Zoltán Erdélyi. An effective method to calculate atomic movements in 3d objects with tuneable stochasticity (3do-skmf). *Computer Physics Communications*, 258:107609, 2021.
[56] Yongmei M Jin and Armen G Khachaturyan. Atomic density function theory and modeling of microstructure evolution at the atomic scale. *Journal of applied physics*, 100(1):013519, 2006.
[57] Mykola Lavrskyi. *Modélisation en fonctionnelle de la densité atomique des transformations de phases dans le système Fe-C à basse température*. PhD thesis, Normandie Université, 2017.
[58] KX Chen, Pavel A Korzhavyi, G Demange, H Zapolsky, Renaud Patte, Julien Boisse, and ZD Wang. Morphological instability of iron-rich precipitates in CuFeCo alloys. *Acta Materialia*, 163:55–67, 2019.
[59] J Zarestky and C Stassis. Lattice dynamics of γ-fe. *Physical Review B*, 35(9):4500, 1987.
[60] David R Lide. *CRC handbook of chemistry and physics*, volume 85. CRC press, 2004.
[61] Shushan Cui, Jianfeng Wan, Xunwei Zuo, Nailu Chen, Jihua Zhang, and Yonghua Rong. Three-dimensional, non-isothermal phase-field modeling of thermally and stress-induced martensitic transformations in shape memory alloys. *International*

Journal of Solids and Structures, 109:1–11, 2017.
[62] Hamed Babaei and Valery I Levitas. Finite-strain scale-free phase-field approach to multivariant martensitic phase transformations with stress-dependent effective thresholds. *Journal of the Mechanics and Physics of Solids*, 144:104114, 2020.
[63] G Demange, M Chamaillard, H Zapolsky, M Lavrskyi, A Vaugeois, L Luneville, D Simeone, and Renaud Patte. Generalization of the fourier-spectral eyre scheme for the phase-field equations: Application to self-assembly dynamics in materials. *Computational Materials Science*, 144:11–22, 2018.
[64] Matteo Frigo and Steven G Johnson. The design and implementation of fftw3. *Proceedings of the IEEE*, 93(2):216–231, 2005.
[65] Berni J Alder and Thomas Everett Wainwright. Studies in molecular dynamics. i. general method. *The Journal of Chemical Physics*, 31(2):459–466, 1959.
[66] ME Agelmenev. The modeling with free boundary. *Molecular Crystals and Liquid Crystals*, 545(1):190–1414, 2011.
[67] A. Goryaeva. fratons2atoms. https://github.com/agoryaeva/fratons2atoms, 2021.
[68] John Douglas Eshelby. The determination of the elastic field of an ellipsoidal inclusion, and related problems. *Proceedings of the royal society of London. Series A. Mathematical and physical sciences*, 241(1226):376–396, 1957.
[69] F Fitzgibbon and Pilu AW. In *B "Direct least squares fitting of ellipses," In Proc. of the 13th International Conference on Pattern Recognition, Vienna*, pages 253–257, 1996.
[70] George Krauss. *Steels: processing, structure, and performance*. Asm International, 2015.
[71] Zenji Nishiyama. *Martensitic transformation*. Elsevier, 2012.
[72] BPJ Sandvik and CM Wayman. Characteristics of lath martensite: Part i. crystallographic and substructural features. *Metallurgical transactions A*, 14(4):809–822, 1983.
[73] Patrick M Kelly. Crystallography of lath martensite in steels. *Materials Transactions, JIM*, 33(3):235–242, 1992.
[74] John Wyrill Christian and Subhash Mahajan. Deformation twinning. *Progress in materials science*, 39(1-2):1–157, 1995.
[75] Ryoichi Monzen and Masaharu Kato. Face-centred cubic to body-centred cubic martensitic transformation of fe-co particles in a copper matrix. *Journal of materials science letters*, 11(1):56–58, 1992.
[76] Tuyen D Le, IM Bernstein, and S Mahajan. Effects of hydrogen on micro-twinning in a FeTiC alloy. *Acta metallurgica et materialia*, 41(12):3363–3379, 1993.
[77] Bruce Alexander Bilby and AG Crocker. The theory of the crystallography of deformation twinning. *Proceedings of the Royal Society of London. Series A. Mathematical and Physical Sciences*, 288(1413):240–255, 1965.
[78] V Vitek, RC Perrin, and DK Bowen. The core structure of $1/2\langle 111\rangle$ screw dislocations in bcc crystals. *Philosophical Magazine*, 21(173):1049–1073, 1970.
[79] PD Bristowe and AG Crocker. Zonal twinning dislocations in body centred cubic crystals. *Philosophical Magazine*, 33(2):357–362, 1976.
[80] PD Bristowe and AG Crocker. A computer simulation study of the structure of twinning dislocations in body centred cubic metals. *Acta Metallurgica*, 25(11):1363–1371, 1977.
[81] Zhe Shi and Chandra Veer Singh. Competing twinning mechanisms in body-centered cubic metallic nanowires. *Scripta Materialia*, 113:214–217, 2016.
[82] PC Rowlands, EO Fearon, and M Bevis. The application of the kossel technique and electron microscopy to the study of the microstructure of Fe-32% ni martensite crystals. *Journal of Materials Science*, 5(9):769–776, 1970.
[83] AG Khachaturyan, SM Shapiro, and S Semenovskaya. Adaptive phase formation in martensitic transformation. *Physical Review B*, 43(13):10832, 1991.
[84] Hiromoto Kitahara, Rintaro Ueji, Nobuhiro Tsuji, and Yoritoshi Minamino. Crystallographic features of lath martensite in low-carbon steel. *Acta materialia*, 54(5):1279–1288, 2006.

Appendix A. Elastic constants used in this work

	C_{11} (r.u.)	C_{12} (r.u.)	C_{44} (r.u.)	B (r.u.)	A_{Zn}	$B^{\mathrm{bcc}}/B^{\mathrm{fcc}}$
bcc	0.23	0.10	0.086	0.14	1.3	1.4
fcc	0.14	0.081	0.090	0.10	3.1	

Table A.2: Elastic constants (in reduced units) of the bcc and fcc structures obtained for the present setting of parameters (see table 1). Zerner anisotropy constant A_{Zn} and the ratio $B^{\mathrm{bcc}}/B^{\mathrm{fcc}}$ between bulk moduli is also provided.

Appendix B. Rotational matrices for KS OR V_1 and V_2

Rotational matrix J_1 (resp. J_2) that transforms the coordinate system of the parent fcc lattice into the bcc lattice with KS OR V_1 (resp. V_2) reads [84]:

$$J_1 = \begin{pmatrix} 0.742 & -0.667 & -0.075 \\ 0.650 & 0.742 & -0.167 \\ 0.167 & 0.075 & 0.983 \end{pmatrix}, \quad J_2 = \begin{pmatrix} 0.075 & 0.667 & -0.742 \\ -0.167 & 0.742 & 0.650 \\ 0.983 & 0.075 & 0.167 \end{pmatrix}$$

Appendix C. Experimental conditions

In this work, the microstructural evolution during casting of a Cu-2.0Fe-0.5Co (wt. %) alloy was investigated via transmission electron microscopy (TEM). The alloy was prepared from high purity Cu, Fe and Co (purity of 99.99, 99.50, 99.95 wt. %, respectively) and elaborated by gravity casting in a vacuum chamber with a medium frequency electrical furnace. A 50 mm × 65 mm × 195 mm cuboid specimen was cast after a homogenization at 1300°C for 20 minutes, followed by an isothermal holding at 1150-1200°C. Thin TEM foils were prepared from 3 mm diameter discs that were mechanically polished and electronically thinned by low-energy Ar milling.

TEM and HRTEM characterization was carried out under JEM-2100F Field Emission Electron Microscope. The TEM and HRTEM images were further processed by DigitalMicrograph 3.5 and Gatan Microscopy Suite 2.1 software. The thickness of twin domains within Fe-rich precipitates were measured and determined from the TEM and HRTEM images, and at least 100 twin domains were analyzed for quantification.

ACKNOWLEDGMENTS

Part of this work was performed using computing resources of CRIANN (Normandy, France) where simulations were performed as Project No. 2012008. This work was supported by the Agence Nationale de la Recherche (contract C-TRAM ANR-18-CE92-0021), the Beijing Municipal Natural Science Foundation (No. 2214072), and the China Postdoctoral Science Foundation (2019M660451).

AUTHOR CONTRIBUTIONS

G. Demange, M. Lavrskyi, R. Patte and H. Zapolsky developed the QA model. G. Demange performed the simulations. K. Chen, J. Hu, X. Chen and Z. Wang performed the preparation of experimental samples and TEM/HRTEM observations. All authors participated in the redaction of the manuscript.

COMPETING INTERESTS

The authors declare no financial and/or non-financial competing interests.

CORRESPONDING AUTHORS

Correspondence to Zidong Wang and Gilles Demange.

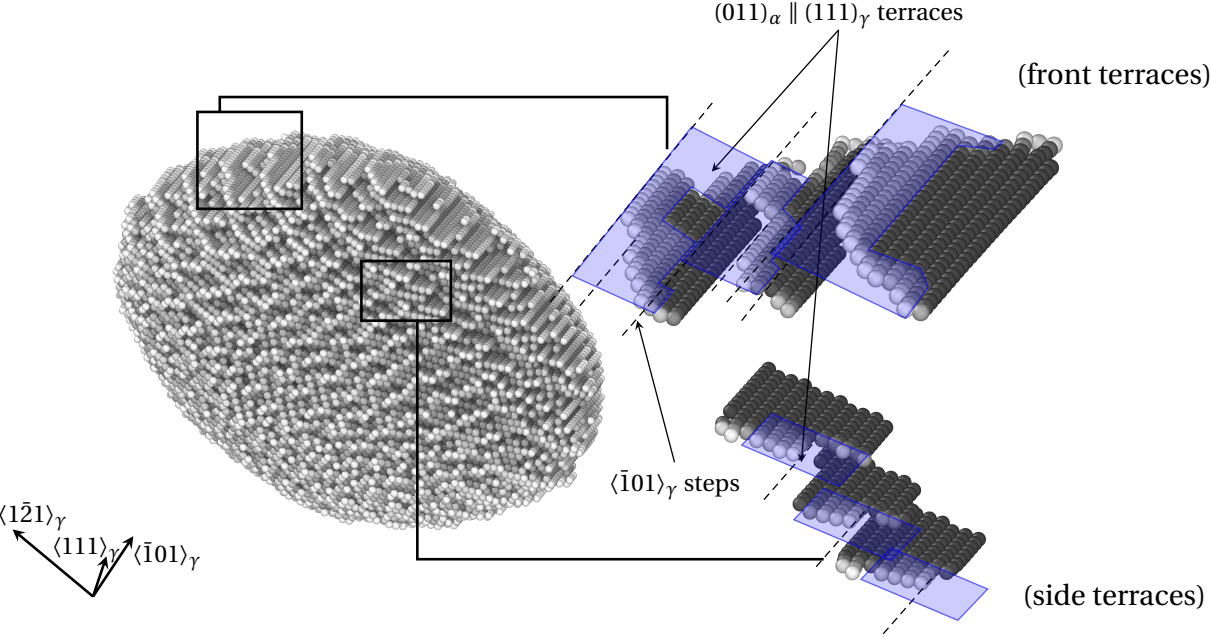

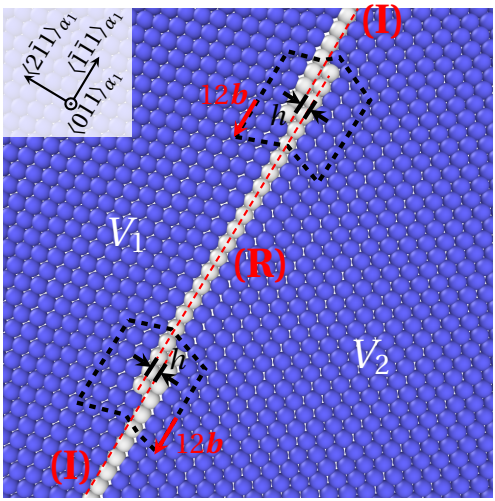

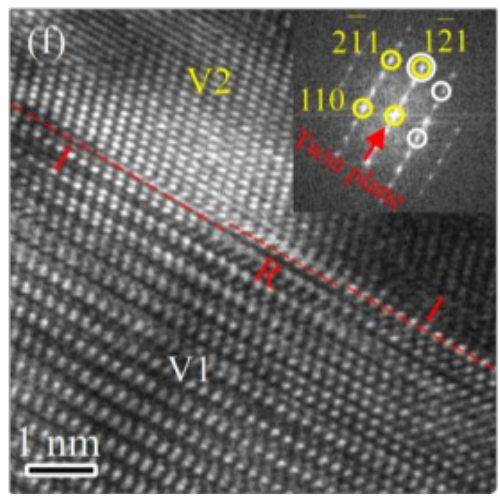

Graphical abstract 1 – *Top : surface relief of a bcc inclusion in a precipitate/matrix binary system, as simulated by the Quasi-Particles (QA) model. Bottom left : partial twin dislocation (TB) couple (IR+RI) with burgers vector* $\boldsymbol{b} = \frac{1}{12}\langle\bar{1}\bar{1}1\rangle_{\alpha_1}$ *and connected by a strip of reflection twin boundary (R) between two twinning domains with Kurdjumov-Sachs orientation relationship (same QA simulation as above). Bottom right : HRTEM micrograph along* $\langle\bar{1}13\rangle_\alpha$ *zone axis, showing similar twinning domains and TB structure, in one spherical Iron-rich nanoparticle.*